University of Zurich[UZH]

Calibration of the first dual-phase xenon time projection chamber with silicon photomultiplier readout

Bachelor's Thesis

Professor:
Prof. Dr. Laura Baudis

Supervision:
Kevin Thieme, Dr. Patricia Sanchez

Student:
Stefan Hochrein

Date:
August 7, 2019

Acknowledgements

At this point I want to thank Prof. Laura Baudis and her kind group for giving me the opportunity to work on this interesting topic. I specially want to thank my supervisors Dr. Paricia Sanchez and Kevin Thieme for their support and advice during my work and for always having a couple of minutes to answer my questions. Thanks to you, I learned a lot during this project. I also want to thank Julian Wulf for setting up the wiki page for me by which I could orientate myself during the thesis, Yanina Biondi for helping me setting up the Jupyter Notebook and Frédéric Girard for the nice image of the Xurich II detector.
Finally, I also want to thank my girlfriend, family and friends for the support besides the work.

Contents

1 Introduction

The dark matter problem is one of the biggest unsolved mysteries of our universe. First hints for dark matter date back almost hundred years. Around 1930 the Swiss-American astronomer Fritz Zwicky observed the velocities of galaxies in the Coma Cluster and found out, that the mass density of the observed cluster is much larger than what was estimated from its luminosity [1]. The additional "invisible" mass, which does not couple to the electromagnetic and strong force, was then called dark matter. Later measurements showed that about 27% of the energy density in the universe are made from cold dark matter while only about 5% are made of baryonic matter [2].
Today the existence of particle dark matter is widely undisputed among scientist even though a direct measurement was not achieved to this date. But new experiments are steadily pushing down the detection limits. One of the most promising approaches to directly detect the interaction of dark matter with baryonic matter via the weak interaction, are the liquid noble gas time projection chambers (TPCs). The idea is to measure the light emitted in an interaction of a dark matter particle with the nucleus of a atom. Current experiments use photomultiplier tubes (PMTs) to detect this light. PMTs have the advantage of a high detection efficiency and gain as well as a low dark count rate but they are rather expensive, bulky and need high voltage. Silicon photomultipliers (SiPMs) are newer devices and have some advantages compared to PMTs. They provide low radioactivity, compact structure, need low operation voltage and are relatively low priced [3]. The main disadvantage of SiPMs so far is their high dark count rate of about $0.82\,\mathrm{Hz/mm^2}$ compared to a typical PMT dark count rate of $0.01\,\mathrm{Hz/mm^2}$ at a TPC working temperature of 172 K [4]. Currently there is a lot of ongoing R&D on SiPMs and motivated by their low radioactivity they are considered an interesting alternative for future dark matter experiments like DARWIN [5].
The work presented in this thesis focuses on the use of SiPMs in a dual-phase xenon TPC and its calibration. This thesis first gives an introduction about dark matter and dark matter detection experiments in chapter 2. Then in chapter 3 the first dual-phase TPC with SiPM readout called Xurich II is introduced and in chapter 4 the process of calibrating Xurich II, and estimating its light and charge yield as well as the detector response parameters $g1$ and $g2$ with a krypton source, is shown. Finally, in chapter 5 the results are discussed and compared to earlier results, achieved with a PMT instead of the SiPMs.

2 Dark matter research

Since Zwicky's observation, new hints for dark matter from novel experiments benefiting from better technical capabilities appeared over time - mostly in astrophysics. This progress also led to efforts to develop a theoretical framework, as well as to attempts to directly detect dark matter. In the following, some of the most important evidences for dark matter, the most promising dark matter candidates, and some detection experiments are introduced.

2.1 Hints for dark matter

2.1.1 Rotation of galaxies

The oldest evidence of dark matter comes from the observation of galaxies, and was first measured in 1933 by Fritz Zwicky on the Coma Cluster [1]. The idea behind this method is to estimate the mass of the cluster in two different ways. The first method uses the virial theorem, and takes into account the whole mass, which interacts through gravitation. The virial theorem states, that regardless of the details of a cluster or galaxy, one can estimate the kinetic energy stored in the whole system to be twice the gravitational energy [6]:

$$\langle E_{kin} \rangle = -\frac{1}{2} \langle E_{grav} \rangle \ \rightarrow \ \frac{1}{2} \cdot M_{\text{tot}} \cdot v^2 = \frac{1}{2} \cdot \frac{\alpha \cdot G \cdot M_{\text{tot}}^2}{R_{\text{tot}}} \tag{2.1}$$

In this formula α is a factor that accounts for the mass distribution and can take values from 0.5 - 2 [1]. The formula can then easily be solved for the total mass of the galaxy M_{tot}, obtaining

$$M_{\text{tot}} \simeq \frac{\alpha \cdot R_{\text{tot}} \cdot v^2}{G}. \tag{2.2}$$

Measuring the overall extent of the system R_{tot} and the mean square of the velocities v, a rough estimate of M_{tot} can easily be calculated.
The second method estimates the mass based on the luminosity of the galaxies and, hence, only takes into account the part of the mass that also interacts through the electromagnetic force. Stars of the main sequence, which are a large percentage of the stars, are observed to have a mass-luminosity relation of [7]:

$$L \propto M^{3.5}. \tag{2.3}$$

The first estimation gives a mass hundreds of times bigger than the second estimation, meaning that a large fraction of the the galaxies' mass is not stored in stars, but in invisible dark matter.

[1] For example, an object with constant density has $\alpha = 3/5$ [6].

A closely related evidence for dark matter was found by Vera Rubin analysing the rotation velocity of stars in disk galaxies [8]. From Newtonian mechanics, it is known that the orbital velocity v_{orb} is related to the mass M enclosed by the orbit through

$$v_{\text{orb}}(r) = \sqrt{\frac{G \cdot M(r)}{r}}. \tag{2.4}$$

The orbital velocity v_{orb} as a function of the distance r to the center of the galaxy was measured by analysing the redshift of single stars. This was done for multiple galaxies. The result for the galaxy NGC 6053 is illustrated in figure 1. It can be seen, that v_{orb} at large radii is almost constant even though the stellar density falls of exponentially. From the discrepancy between the measured and calculated velocity the density of the dark matter halo was calculated [9].

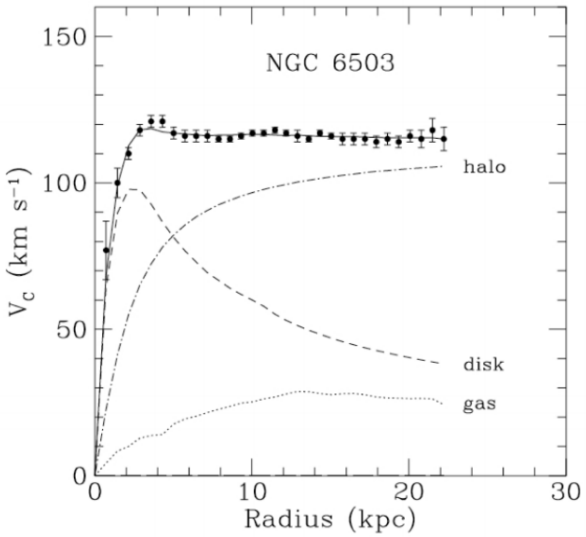

Figure 1: Measured orbital velocities v_{orb} in the galaxy NGC 6053 as a function of the radius r. The velocity parts caused by the different components of the galaxy are also shown. Figure from [9].

2.1.2 Gravitational lensing

In 2006 the team around Douglas Clowe found a hint for the existence of dark matter in the Bullet Cluster merger using the effect of gravitational lensing. Gravitational lensing is caused by the deflection of light trajectories by large masses, described by Einstein's theory of general relativity [10]. It can be observed if large masses (stars, galaxies or clusters of galaxies) pass in between the observer and stars further away.
The idea behind this technique was again to calculate the mass distribution in two

different ways. The gas clouds of the two clusters heat up by the collision and start to emit X-rays. The clouds are the dominant baryonic mass components and they can be localised, detecting the X-rays. Additionally, using the effect of gravitational lensing, a map showing the gravitational potential can be calculated. In figure 2 the result of this procedure is shown. It can be seen that the gravitational lensing map, showing the gravitational potential, does not trace the gas distribution [11].

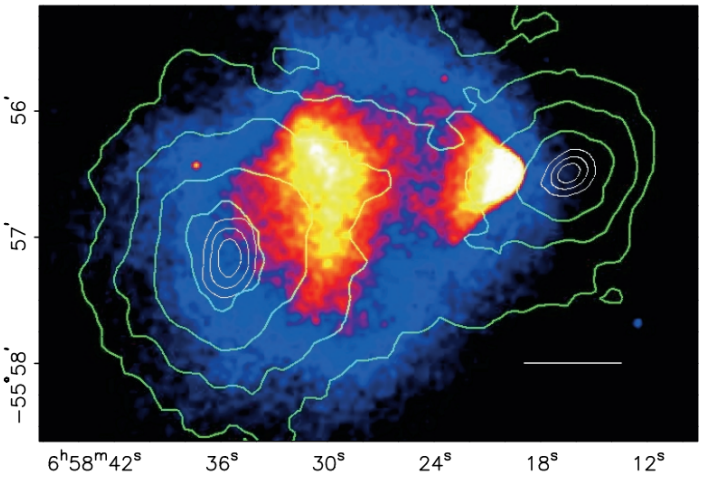

Figure 2: Image of the unique cluster merger 1E 0657-558. The green contour lines show the gravitational potential calculated from gravitational lensing, the heat map shows the distribution of the gas clouds. Figure from [11].

2.1.3 Cosmic microwave background radiation

Today one of the strongest indications for dark matter comes from the exact measurement of the cosmic microwave background (CMB) radiation. Shortly after the big bang, the young universe was a hot and dense plasma in a nearly perfect thermal equilibrium. After roughly 380 000 years the universe cooled down enough, such that the formed helium atoms were not fissured anymore. At this point, which today is referred to as recombination era, the universe became transparent to light. The radiation released during recombination is now called the CMB and it can be detected precisely in satellite based experiments, such as COBE [12], WMAP [13] and Planck [14]. The Planck result is shown in figure 3. Analysing Planck data, it was found that the CMB is very uniform but it has small fluctuations imprinted at the order of 10^{-5} [15]. These fluctuations were caused by acoustic, i.e., pressure waves in the early universe. The pressure waves were only transported by ordinary matter but not by dark matter. Measuring the exact size of the fluctuations, it is possible to make conclusions on the matter composition in the early universe. Based on CMB data and other observations the standard cosmological

model (ΛCDM model) has been developed. Fitting the model to the CMB data showed that only 5% of the universe consist of baryonic matter, while 27% consist of dark matter and 68% consist of dark energy, which is responsible for the ongoing acceleration of the expansion rate of the universe [16].

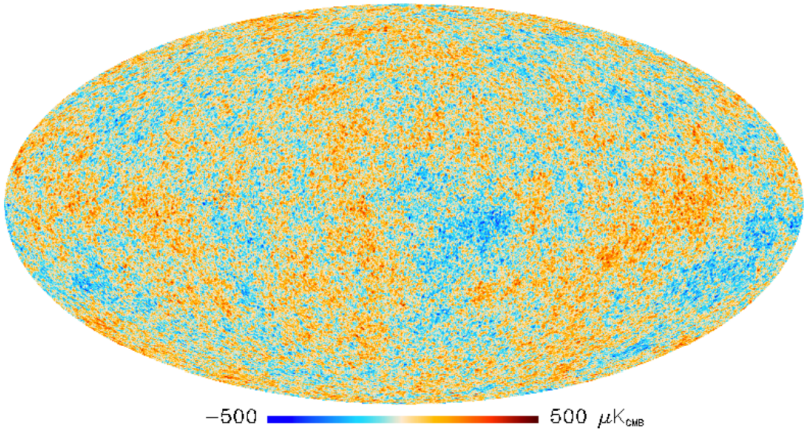

Figure 3: Map of the CMB radiation, measured by the Planck satellite. The red areas have a slightly higher temperature, than the average CMB temperature of 2.725 K [17], the blue areas a lower one. Figure from [14].

2.2 Dark matter properties and candidates

While the properties of dark matter from direct detection experiments are still unknown, there are already a lot of cosmological constraints that dark matter has to fulfil. First of all, as the name already indicates, dark matter has to be optically dark, which means that it carries no or very little electric charge or magnetic dipole moment. This means that dark matter does not radiate, cool down and collapse into the center of galaxies like baryons. Nevertheless, dark matter is observed to be bound to galaxies, therefore it needs to be sufficiently slow (i.e., non relativistic). In addition, dark matter has to be stable on the time scale of the age of the universe, since its presence can be observed from recombination in the CMB up until now in galaxies. Today, the local dark matter density is estimated to be (0.2−0.46) GeV/cm^3. Further, dark matter has to be almost collisionless, because the self interaction would make the dark matter halo of galaxies round, in contrast to the observations. The heavier dark matter particles are, the lower is the needed dark matter particle density, and the stronger can the self interaction be. Thus, the important quantity is the mass to self interaction cross section ratio. However, dark matter particles can not be arbitrary heavy because too heavy particles would disrupt bound orbits, which is not observed. Finally, dark matter can be classified in two main categories, hot or cold dark matter. In the hot dark matter scenario, clusters

formed first and then broke apart into galaxies while in the cold dark matter scenario instead, galaxies formed first and later merged to clusters [2].
A candidate for the hot dark matter scenario would be the neutrino, which interacts, besides gravitation, only through the weak interaction. Measurements showed that the neutrino mass is very small [2], making it a weakly interacting light particle (WILP). However, the hot dark matter scenario seems to be against astronomical observations [19].
For the cold dark matter scenario, weakly interacting massive particles (WIMPs) or axions are the best candidates.

2.2.1 WIMPs

WIMPs would be a new particle species that, like neutrinos, only interact through gravitation and the weak interaction, or a new even weaker interaction, but with a much larger mass in the range from 1 GeV to 10 TeV [20]. WIMPs arise naturally in different theories beyond the standard model, like in theories with extra dimensions where the WIMP would be the so called Kaluza-Klein particle, or supersymmetric extensions of the standard model, where it would be the lightest supersymmetric particle [2].

2.2.2 Axions

Axions were first introduced to solve the CP problem in quantum chromo dynamics (QCD) as so called Nambu-Goldstone bosons. They are associated to the global symmetry breaking and their mass is linked to the symmetry breaking scale f_a. For example if f_a is in the range between 100 GeV and 10^{19} GeV, the axion mass is between 1 MeV and 10^{-12} eV [2]. However, for the symmetry breaking around the electroweak scale, the corresponding axion mass, around 200 keV, was already excluded by measurements, leaving only heavy or light possible axions masses.

2.3 Dark matter detection experiments

To confirm the ΛCDM model, the existence of dark matter has to be proven. The goal is further to measure the properties of dark matter, such as the mass and the coupling, and to extend the standard model of particle physics. There are different possibilities of how this can be achieved, displayed in figure 4. Indirect detection experiments try to measure particles produced in dark matter annihilation, while collider experiments look for the exactly opposite process. Direct detection experiments aim for the measurement of a scattering process between dark matter and baryonic matter. In the following an overview of current dark matter detection experiments is given.

[2] Sum of the three neutrino masses is less than 0.32 eV. [18]

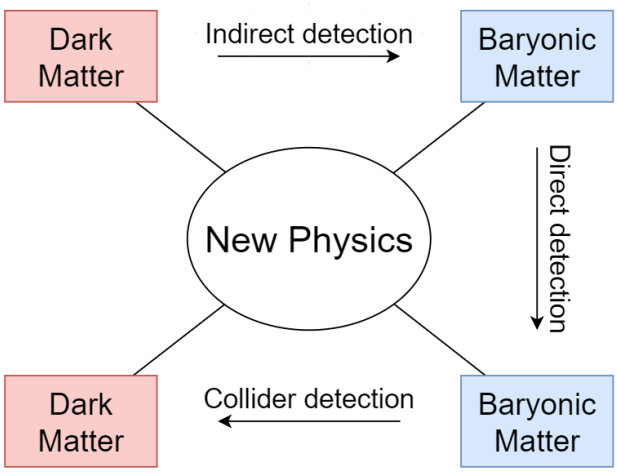

Figure 4: Diagram of dark matter detection possibilities. The diagram has to be read as a Feynman diagram with the arrows as the time axis.

2.3.1 Indirect detection

Indirect detection looks for the products of a dark matter annihilation reaction. These reactions are expected to mainly take place in regions with a high dark matter density, for example in other galaxies or in the center of the sun or milky way. The spectrum of possible annihilation products is quite wide. Potentially produced particles to look for are γ-rays, neutrinos, positrons and antiprotons [21]. A schematic overview of different indirect dark matter detection techniques and experiments, together with the particles they can measure, is shown in figure 5.
Low energy γ-rays often do not reach the earth, and are therefore detected using satellite based space telescopes. The γ-rays produce electron-positron pairs in the detector, which can be tracked. The energy is then measured in a calorimeter. An example of such an experiment is Fermi-LAT [22].
High energy γ-rays are detected by ground based Cherenkov telescopes. When high energetic γ-rays hit the atmosphere, electron-positron pairs are produced. If these particles have enough energy to travel faster than the speed of light in the medium (atmosphere), they emit Cherenkov light [23]. By detecting the light in an array of telescopes, the direction and energy of the incident photon can be calculated to find its source. Examples of such experiments are HESS [24], MAGIC [25], VERITAS [26] and the not yet operating CTA [27].
Neutrinos are also detected using Cherenkov light. However, to detect neutrinos, detectors need to have a large target mass because of the small interaction cross section of the neutrinos with nucleons and electrons. Most neutrino detectors are water- or ice-based. Examples are Super-Kamiokande [28] and ICECube [29].

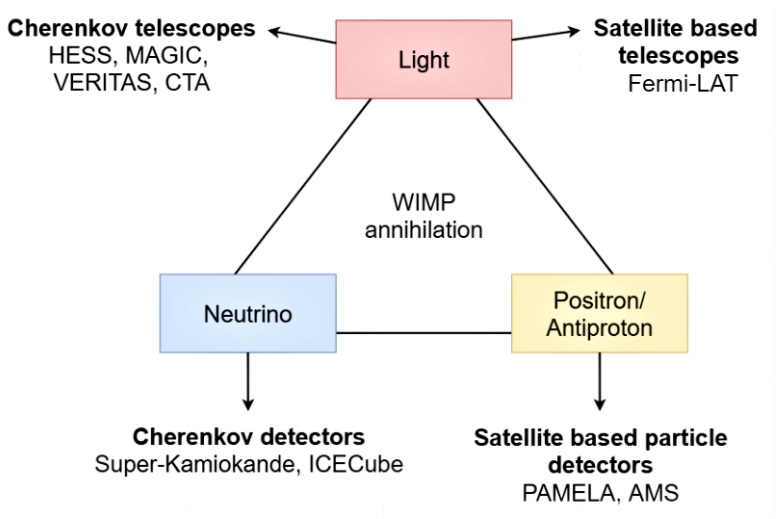

Figure 5: Overview of indirect dark matter detection techniques and the particles they try to measure. Some examples of experiments are listed too.

Cosmic positrons and antiprotons do not reach the earth because of the magnetic field and the atmosphere. Therefore, satellite based detectors are used as for low energy γ-rays. Examples of such experiments are PAMELA [30] and AMS [31]. PAMELA and AMS found an excess in the positron/electron ratio which could be explained by dark matter annihilation but a stronger significance is needed before any signal claim [32].

2.3.2 Production at collider experiments

Theoretically, dark matter could be produced in high energy particle collisions. In experiments, such as ATLAS or CMS at the Large Hadron Collider (LHC), WIMPs would show up as missing transverse energy/momentum in an event [33]. Collider data could mainly be used to determine WIMP masses, but it is not very sensitive to its scattering cross section [20]. The advantage of collider experiments is that they do not suffer from astrophysical uncertainties such as the dark matter density. Unfortunately, this is a disadvantage at the same time, because even if WIMPs are found in collider experiments, the existence of the galactic dark matter halo would still have to be proven.

2.3.3 Direct detection

The goal of the direct detection is to measure the nuclear recoil caused by the elastic scattering with a WIMP. The idea is that the deposited energy in the interaction is transformed into a measurable signal such as scintillation light, charge or heat [20]. The biggest problem is the very small expected event rate which has to be distinguished

from the background. Most experiments use more than one signal at once to achieve a better background discrimination. A schematic overview of different direct dark matter detection techniques and experiments, together with the signals that they can measure, is shown in figure 6.

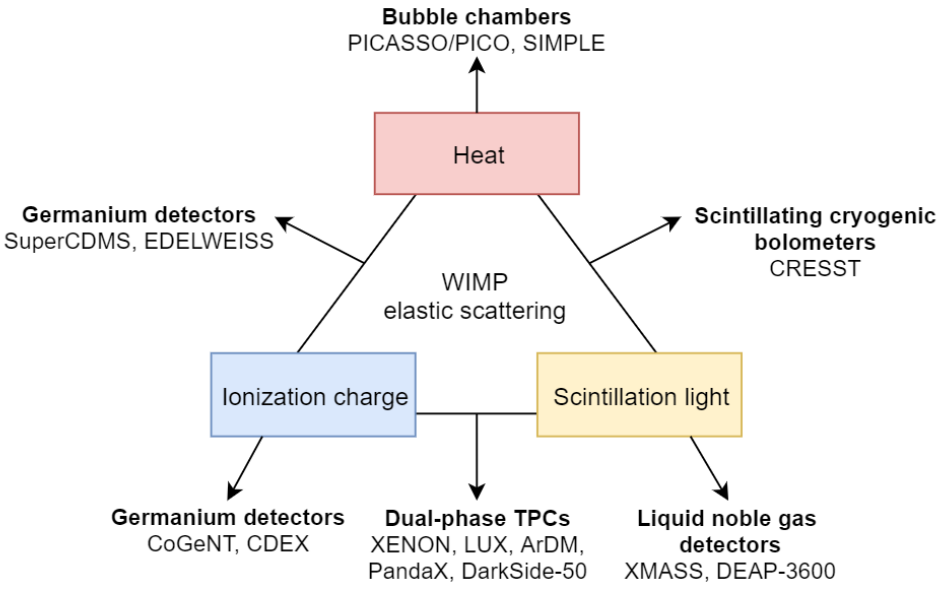

Figure 6: Overview of direct dark matter detection techniques and the signal they use. In addition some examples of experiments are listed.

The first limits on the WIMP-nucleon cross section have been obtained in experiments that measure ionization signals in germanium crystals as target material. The advantages of these crystals are the low energy threshold and the high energy resolution. Example of germanium based experiment that measures ionisation charge are CoGeNT [34] and CDEX [35]. Other experiments, such as SuperCDMS [36] and EDELWEISS [37], additionally measure phonons in germanium crystals.
Another group of experiments measure small amounts of deposited heat in bubble chambers to search for dark matter. They use superheated liquids in which a tiny amount of energy is enough to change the aggregation state to gaseous. Examples are PICASSO [38], its follow-up project PICO [39] and SIMPLE [40].
The experiment CRESST [41] aims for measuring heat in the form of phonons and scintillation light in a cryogenic bolometer made of a $CaWO_4$ crystal.
The most promising subgroup of direct detection experiments use noble gas elements, such as argon and xenon as target material. Besides the low radioactivity, they have the advantage to have a high density as well as a good self shielding, and good scintillation and charge yields. Some experiments, like XMASS [42] and DEAP-3600 [43] use the scintillation light only. Other experiments like XENON [44], LUX [45], PandaX [46],

DarkSide-50 [47] and ArDM [48] are based on dual-phase detectors that can also measure ionisation charge. In chapter 3, the working principle of a dual-phase liquid xenon detector is described in detail. The XENON1T experiment has the best exclusion limit for the spin-independent WIMP-nucleon cross section up until now [49]. An advantage of xenon over argon is that the xenon scintillation light is directly measurable, while for argon wavelength shifters have to be used. Moreover, natural xenon contains isotopes with an uneven nucleon number, and therefore allows the search for spin-dependent interactions. The parameter space covered by XENON1T and other experiments described above, is shown in figure 7.

2.3.4 Future direct dark matter experiments

Several new experiments are planned to cover the whole parameter space, possible WIMP masses span. In the near future the follow-up experiments of XENON1T, LUX and DarkSide-50 called XENONnT [50], LZ [51] and DarkSide-20k [52] respectively will start taking data and presumably increase the current sensitivity by an order of magnitude. Finally, DARWIN [5], a proposed next generation xenon experiment, will cover all WIMP masses above 5 GeV down to the irreducible coherent neutrino-nucleus scattering floor, as illustrated in figure 7. This goal should mainly be reached by building a detector with much larger target mass and achieving an unprecedented ultra-low background level.

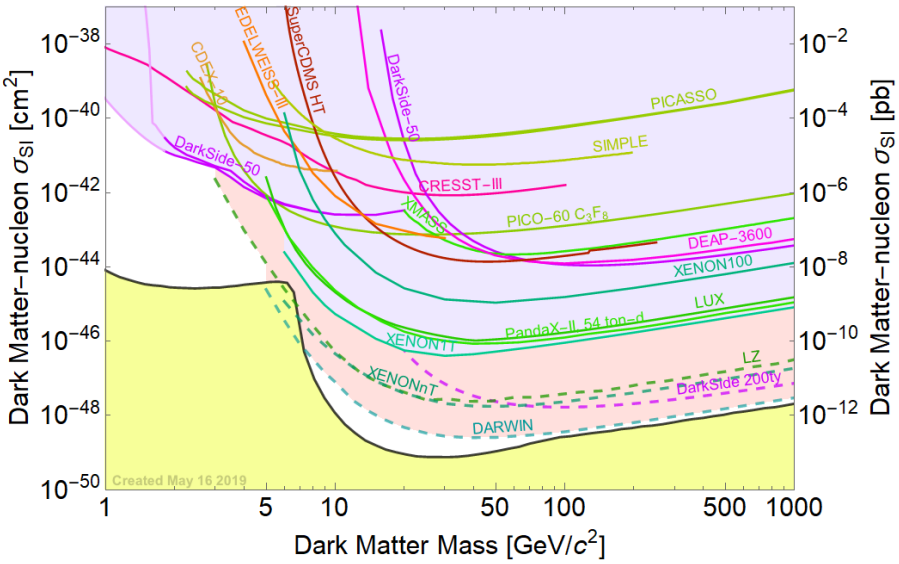

Figure 7: The selected direct dark matter detection experiments from above, and the parameter space they cover. The neutrino background is marked in yellow, while the already excluded parameter space is marked in blue. The parameter space which DARWIN will cover is marked in red. Figure created with the Dark Matter Limit Plotter from T. Saab and E. Figueroa.

3 Xurich II with SiPMs

In this chapter the general working principle of a dual-phase xenon TPC is explained. The first dual-phase TPC with SiPM readout called Xurich II is introduced and its setup is described in detail with focus on the photosensors. The last section of the chapter describes the properties of the ^{83m}Kr isotope and how it can be used as a calibration source for Xurich II.

3.1 Working principle of a dual-phase TPC

A TPC mainly consists of a cylindrical tank containing a noble gas, such as xenon or argon. In a dual-phase TPC the volume is split into a liquid and a gas phase. On the top and bottom of the TPC photosensors are installed to detect light. Additionally two electric fields are applied in the z-direction, one to accelerate free electrons to the top and the other to extract them into the gas phase, as illustrated in figure 8.

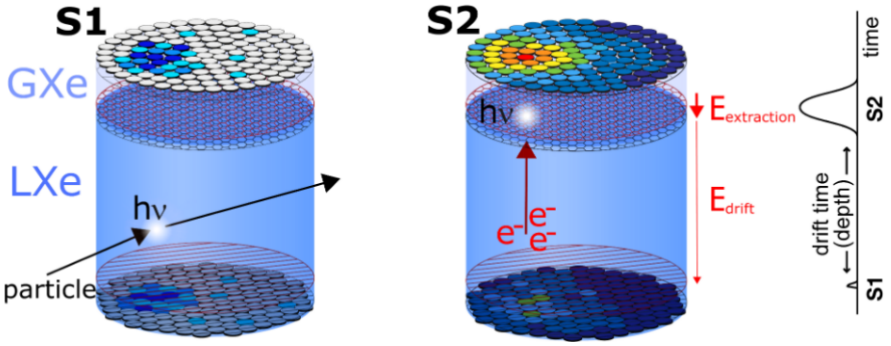

Figure 8: Schematic illustration of the working principle of a dual-phase time projection chamber. LXe stands for liquid xenon while GXe stands for gaseous xenon. Figure from [4].

When a particle interacts inside the TPC it deposits energy, which is split into ionization, excitation and heat. As already mentioned in section 2.3.3, in a TPC the ionization and excitation signal can be measured, while the heat is lost [20].

In the case of a xenon TPC, an ionized xenon atom (Xe^+) forms a bound state with another xenon atom. If this molecule captures a free electron it splits up, releasing heat and forming an excited state (Xe^*):

$$Xe^+ + Xe \rightarrow Xe_2^+, \tag{3.1}$$

$$Xe_2^+ + e^- \rightarrow Xe^{**} + Xe, \tag{3.2}$$

$$Xe^{**} \rightarrow Xe^* + \text{heat}. \tag{3.3}$$

The excited xenon atom, which can also be directly produced in an interaction, forms an excited diatomic molecule with another xenon atom. In the following de-excitation, this molecule releases a photon with a characteristic wavelength of 178 nm:

$$Xe^* + Xe \rightarrow Xe_2^*, \tag{3.4}$$

$$Xe_2^* \rightarrow 2Xe + h\nu. \tag{3.5}$$

In these two ways the prompt scintillation signal is produced (S1 signal). The S1 signal is very fast because the excited states have short decay times of $\mathcal{O}(10\,\text{ns})$ [20].
In the case of ionization, the free electrons are accelerated in the applied electric field and drift up to the gas phase. When the electrons are extracted into the gas phase they again ionize or excite xenon atoms and a second amplified light pulse is emitted, which gives another signal (S2 signal). Because of the longer drifttime of $\mathcal{O}(1\,\mu\text{s})$[1], the S2 signal follows the S1 signal. The delay between the S1 signal and the S2 signal gives the interaction depth (z-position).

[1]This is only the case for the small Xurich II TPC. In general the drifttime depends on the size of the detector as well as on the applied drift field which influences the drift velocity. For large detectors the drifttime can be of $\mathcal{O}(1\,\text{ms})$.

3.2 Xurich II setup

The Xurich II TPC is shown in figure 9. The cylindrical active volume ⑧ has a diameter of 3.1cm and the same height. It is defined by a polytetrafluoroethylene[2] (PTFE) reflector and contains 68 g of liquid xenon. A PMT ⑩ is placed on the bottom of the TPC while an array of 16 small SiPMs ② is installed on the top. A printed circuit board (PCB) ① for the readout is placed right above the SiPMs. More details about the PMT and the SiPMs can be found below.
Three meshes are placed inside the TPC in order to apply the electric field. The cathode ⑨ is located right above the PMT and operates at a negative voltage. The grounded gate ⑤ is installed in the liquid xenon right below the gaseous phase. Finally a few mm above the liquid level, the anode ④ is located. While the drift field between cathode and gate varied for the datasets, the electric field between gate and anode was constantly 10 kV/cm. It needs to be that strong in order to extract electrons into the gas phase. To keep the drift field uniform seven copper field shaping rings ⑥, with a linear potential drop achieved by a chain of resistors, surround the TPC. For a stable two-phase operation, the liquid level can be monitored by three capacitors ③ and regulated by a weir system ⑦ and a motion feedthrough.
The whole TPC is contained within a stainless steel vessel inside a vacuum cryostat. It is cooled by a copper cold finger which is plunged in liquid nitrogen. In order to control the temperature inside the TPC, a 5 W heater is placed on the top of the inner cryostat.

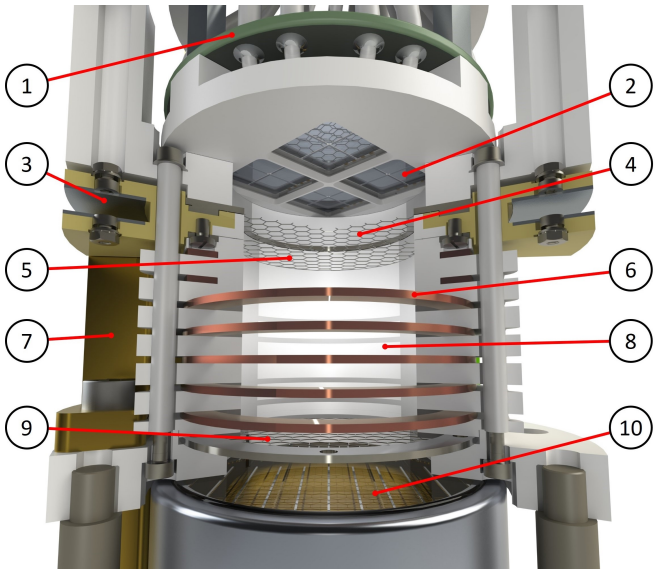

Figure 9: Schematic drawing of Xurich II. Figure credits: Frédéric Girard, Andreas James.

[2]Better known under the brand name Teflon.

The Xurich II detector operates at a temperature of roughly 180 K such that the liquid level and the optimal pressure of 2.0 bar remain stable. The xenon is in a constant circulation through a gas handling and purification system outside the TPC. The gaseous xenon is purified by flowing through a hot metal getter. The gas system is also needed to introduce the ^{83m}Kr calibration source into the xenon gas flow and back into the TPC [53].

3.2.1 PMT

The PMT is of type R9869 from Hamamatsu Photonics, developed for liquid xenon applications. It has a diameter of 2 inch (= 5.08 cm), operates at a voltage of 940 V and has a gain of about 5×10^6. The PMT has a photon-detection efficiency of about 35% [53].
A PMT works in the following way: The incident light falls on the photocathode, where it releases an electron. The electron is then accelerated by a focusing electrode onto an electron multiplier dynode, where it liberates more electrons. This process is repeated several times until a shower of electrons falls onto the anode, where it produces a signal in the voltage. For low enough energies, the size of the signal is proportional to the energy of the incident photon(s) [54]. Figure 10 illustrates the structure and working principle of a PMT.

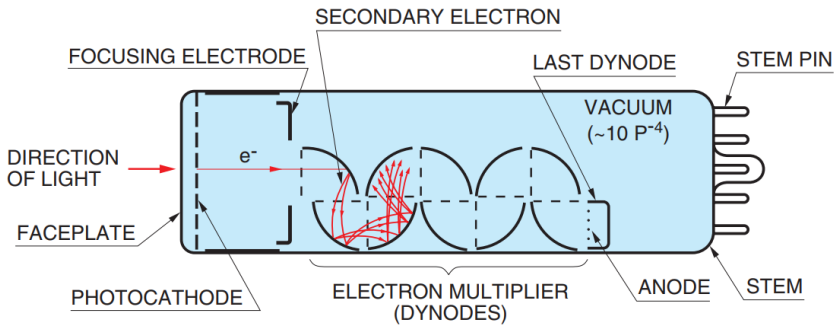

Figure 10: Schematic drawing of a PMT. Figure from [54].

3.2.2 SiPMs

The top array consists of four photosensors type S13371 from Hamamatsu Photonics. Each of them consists of a 2×2 array of $6 \times 6\,\text{mm}^2$ SiPMs. Every SiPM contains 14 400 microcells of each $50 \times 50\,\mu\text{m}^2$. They have a photon-detection efficiency of about 24%, operate at a bias voltage of 51.5 V and have a gain of 31×10^6 [3].
Every microcell consists of an n-doped region above a p-doped region on a silicon substrate, as illustrated in figure 11. The active region of a microcell is at the border between the two regions. If a photon passes this area, an avalanche of $10^5 - 10^6$ electrons is re-

leased. The cells operate in Geiger-mode and the signals of all microcells are summed up in the readout electronics [55]. The main advantage of the SiPMs for Xurich II is their small size, which allows for a good position reconstruction in the x-y plane. More specific details can be found in [3].

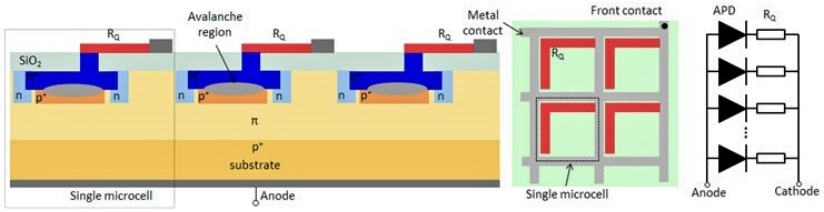

Figure 11: Schematic drawing of the structure of the microcells in a SiPM (left) and the circuit diagram (right). Figure from [55].

3.2.3 Data acquisition

The signal of the PMT is first attenuated by a factor of 10, while the signal from the SiPMs is amplified by the same factor. If the PMT signal exceeds the threshold of 2 mV an event is triggered. If an event is triggered, the signals from the PMT and the SiPMs are digitised by three analog-to-digital converter (ADC) boards. Which SiPMs are connected to which board can be seen in figure 12. The ADCs need to be well synchronized and if they are not the misalignment described in section 4.3 can be observed.

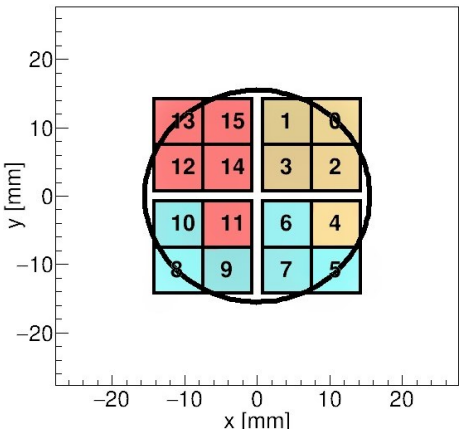

Figure 12: Drawing of the areas covered by the SiPM array. The circle shows the TPC wall. The colors of the SiPMs indicate which SiPMs were digitized together in an ADC board. The PMT was digitized in the same ADC as the SiPMs 0-4. Figure credit: Julian Wulf.

3.3 ^{83m}Kr as a calibration source

^{83m}Kr is often used as a calibration source for TPCs because of its short half life and low-energy lines. It is produced in 76% of the decays of ^{83}Rb, which decays by electron capture with a half life of $T_{1/2} = (86.2 \pm 0.1)$ d. The decay scheme is shown in figure 13 (a).
^{83m}Kr has a half life of $T_{1/2} = (1.83 \pm 0.02)$ h and an energy difference to the stable ^{83}Kr ground state of (41.5575 ± 0.0007) keV. However, ^{83m}Kr does not directly decay into the ground state but via an intermediate state. This state as has a much shorter half life, $T_{1/2} = (156.8 \pm 0.5)$ ns, and an energy difference to the ground state of (9.4057 ± 0.0006) keV. Hence, the corresponding released energies, which can be used for the calibration, are $E_1 = (32.1516 \pm 0.0005)$ keV and $E_2 = (9.4057 \pm 0.0006)$ keV [56].
These decay properties give some important advantages of using krypton as a calibration source in TPCs: First of all, the decay is easily identifiable in a TPC because of its decay in two steps which leads to two S1 signals followed by two S2 signals. The first signal, corresponding to the 32.1 keV line, is larger than the subsequent signal. The topology of a typical event can be seen in figure 13 (b). Secondly, the krypton source can easily be introduced in the TPC by placing a solid ^{83}Rb source (powder) into the xenon gas flow with appropriate filters. Furthermore, the krypton events are homogeneously distributed in the TPC, compared to external calibration sources. Finally, after the calibration the activity of the krypton drops rather fast, such that other data can be taken. The remnant krypton has similar properties than xenon, does not absorb xenon scintillation light and hence does not disturb the performance of the TPC [57].

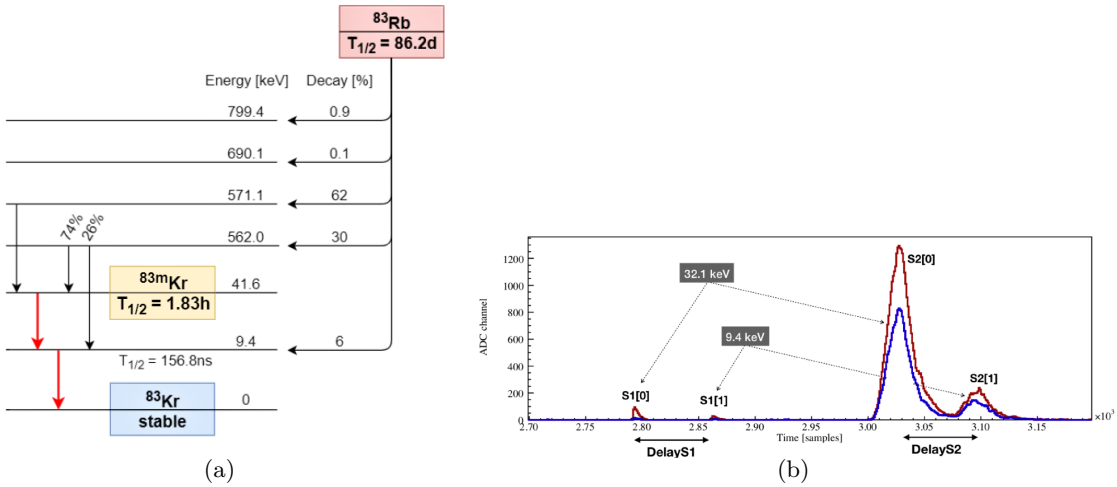

Figure 13: (a): Schematic of the ^{83}Rb decay, the red arrows show the two lines considered for the calibration. (b): Typical krypton event signal detected in a TPC. Figure from [58].

4 Krypton data analysis

4.1 Analysis framework

The analysed data was preprocessed by the WARP-ZERO processor written by Kevin Thieme. This processor scans the digitized waveforms of the PMT and the 16 SiPMs and identifies the largest as well as the second largest S1 and S2 signals. It then stores the important information about them (time position, amplitude, width and area) and additional background information (event time and number, gain of PMT and SiPMs) in a ROOT file.
The data was then post processed by a script provided by Julien Wulf. It identifies coincidences among the channels, selects the important information for the analysis and stores it in the so-called "minitrees" (ROOT files). It also adds for every event the drifttime as well as the position in the x-y plane.
For the following analysis, the "minitrees" were analysed using pandas dataframe as well as numpy, scipy and matplotlib in a python jupyter notebook.

4.2 Position reconstruction

The x-y position of each event was calculated by the script of Julian Wulf from the S2 signals, using the center of mass algorithm. The S2 signal is assumed to lay directly above the event interaction, because the electrons drift parallel to the z-axis along the electric field. Therefore, summing up the coordinates $\vec{x_i}$ of the SiPMs weighted by the number of photoelectrons N_{pe}^i measured by the i-th SiPM, gives the reconstructed position:

$$\vec{x} = \frac{\sum_{i=1}^{16} N_{pe}^i \cdot \vec{x_i}}{\sum_{i=1}^{16} N_{pe}^i}. \tag{4.1}$$

Because of the quadratic geometry of the SiPM array the positions are mapped on a square and biased towards the middle of the detector, as clearly visible in figure 14 (a). Unfortunately the mapping towards the middle is not linear.
To correct the event positions, in a first step, the uncorrected event positions were centred and scaled to a unit square. The unit square was than mapped onto a unit circle, using the elliptical grid mapping [59]:

$$x' = x \cdot \sqrt{1 - \frac{y^2}{2}}, \quad y' = y \cdot \sqrt{1 - \frac{x^2}{2}}. \tag{4.2}$$

The obtained positions were then rescaled to the original size. The result can be found in figure 14 (b).
Fortunately in the center of the detector the resolution of the position reconstruction is good and the knots of the gate mesh, needed to apply the drift field, are clearly

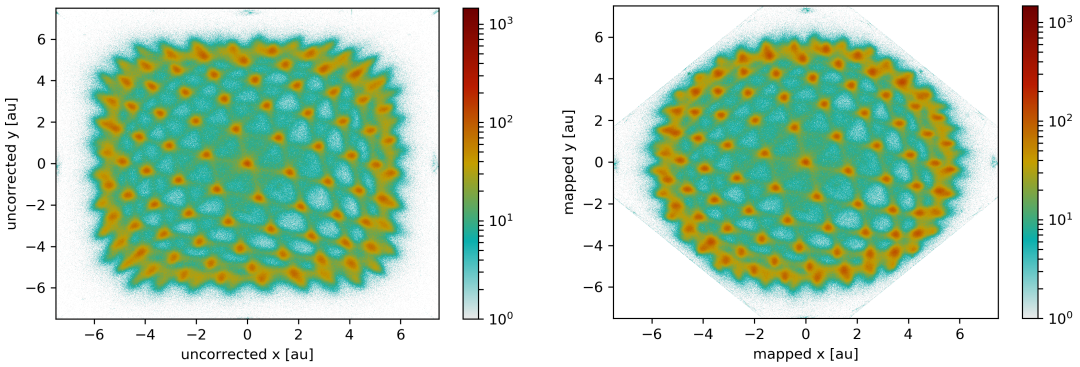

(a) (b)

Figure 14: (a): Event positions calculated by the script of Julian Wulf. (b): Event positions after mapping to a circle.

visible. Comparing the position of the knots in the data with the well known size of the mesh[1], the events can be mapped to the original size of the detector. This was done by first selecting events on two lines going exactly through the knots. The radius of the selected events was then histogrammed and the peaks (knots) were fitted with a Gaussian function. The found peak positions were then plotted against the well known positions of the knots. Finally, a third order polynomial fit was performed through these points in order to extract the non linear scaling factor, as shown in figure 15 (a). The resolution of the knots clearly drops at large radii. The outermost reconstructible knots lay at $r = 9.7\,\text{mm}$. The final result of the position reconstruction can be seen in figure 15 (b).

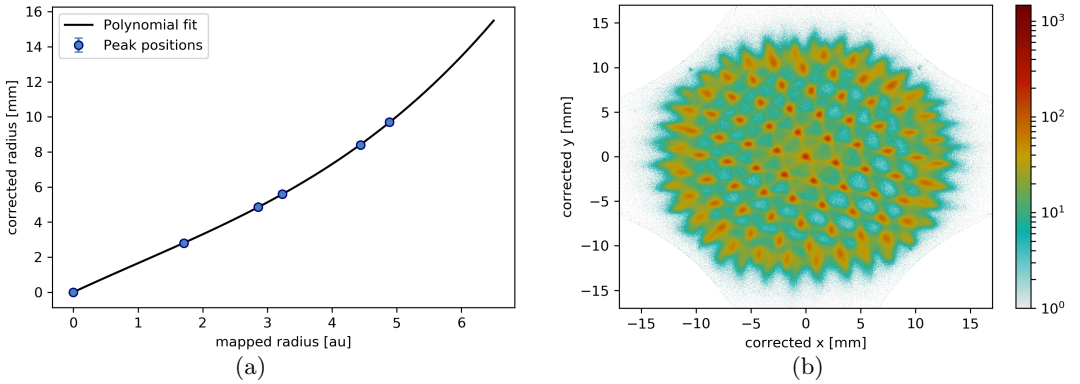

(a) (b)

Figure 15: (a): Fit through the knot positions, with the uncorrected radius on the x-axis and the corrected radius on the y-axis. (b): Corrected event positions.

[1]The real distance between two neighbouring knots is 2.8 mm.

4.3 Data selection

The main goal of the data selection was to identify datasets in which no misalignment (de-synchronisation of the readout boards) occurs. Misalignment between the digitisers can occur if the event rate is too high, such that the boards are overwhelmed. The easiest way to identify these datasets is to histogram all events in the x-y plane. Because of the time offset in a part of the boards the position is incorrectly reconstructed by the center of mass algorithm. The histogram is then not rotationally symmetric anymore and sometimes shows a population of events outside the detector. An example of a dataset with and without the misaligned topology can be seen in figure 16. Out of total 175 datasets, 121 flawless datasets were identified by eye as correct. An overview of all files can be found in table 5 in the appendix.

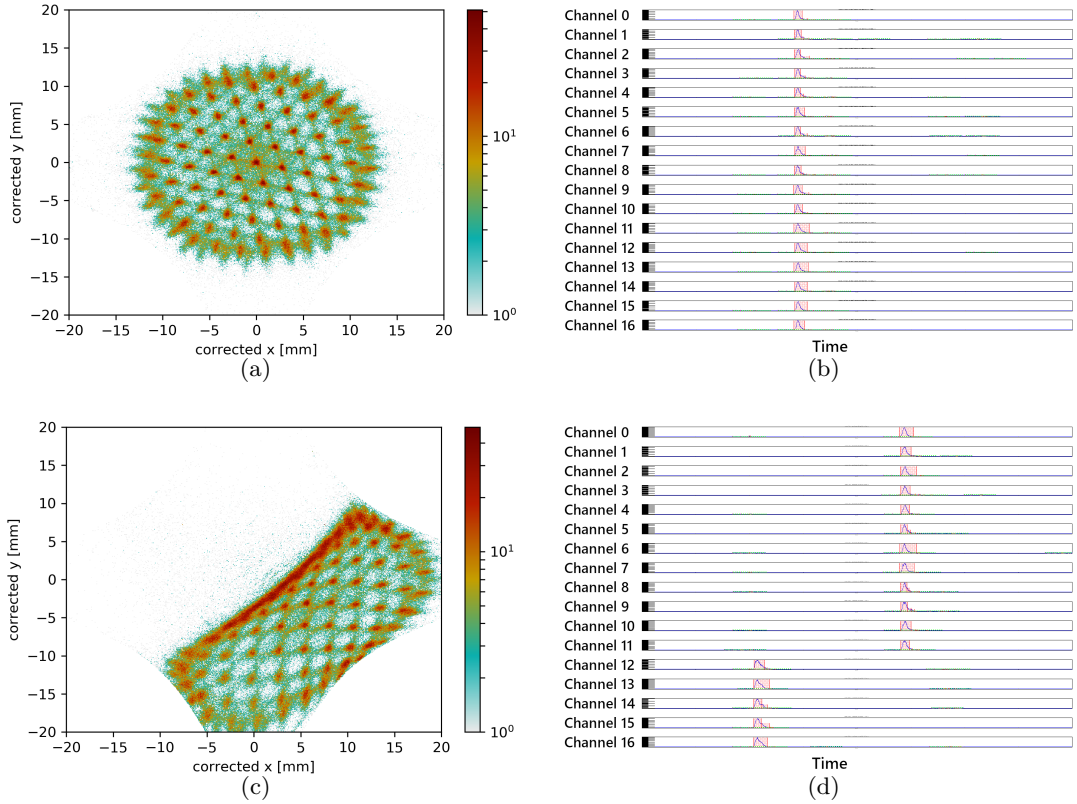

Figure 16: The left figures show the event distribution of a dataset in the x-y plane. The right figures show a typical waveform of an event in the same dataset. (a), (b): Good dataset (190202_1101), no misalignment. (c), (d): Misaligned dataset (190202_1205), ADC module 2 (channel 12-16) misaligned.

4.4 Cuts

One goal of the krypton data analysis is to find out the light and charge yield of the detector. These values are defined as the number of photoelectrons (PE) detected by the PMT and the SiPMs per deposited energy in the detector. To find this value one needs to have a population of events for which the deposited energy is well known, in this case the krypton events. In order to select only krypton events, a basic set of cuts must be applied. The values of the cuts are listed in table 1. For the first two cuts no concrete values are given because they differ for the datasets. The purpose and implementation of every cut is described in the subsections below.

Cut	Lower limit	Upper limit	Efficiency
Time delay	S1 delay - S2 delay $> \mu - \sigma$	S1 delay - S2 delay $< \mu + \sigma$	4%
S2 width	S2 width $> a_0 - b_0 t + \sqrt{c_0 t}$	S2 width $< a_1 - b_1 t + \sqrt{c_1 t}$	62%
Area fraction top	area fraction top > 0.21	area fraction top < 0.31	68%
Fiducial volume	z > -25 mm & r > 0 mm	z < -5 mm & r < 9.7 mm	6%

Table 1: Summary of all applied cuts. The efficiency of a cut is defined as the percentage of events that survive the cut, compared to all events with no cut applied.

4.4.1 Time delay cut

As already mentioned in section 3.3, the ^{83m}Kr isotope decays in two steps with decay times $T_{1/2} = 1.83\,\text{h}$ (32.1 keV) and $T_{1/2} = 156.8\,\text{ns}$ (9.4 keV). Therefore, a krypton event signal shows two S1 as well as two S2 peaks with the same time difference. Thus, plotting the time delay between the S1 peaks against the time delay between the S2 peaks gives the diagonal, as clearly visible in figure 17 (a) and (c). Background events and accidental coincidences instead are randomly distributed and hence do not show this behaviour.
To get the time delay cut a Gaussian fit was performed on the histogrammed delay difference (S1 delay - S2 delay) data and the 1σ interval around the mean was selected as written in formula 4.3. An example can be found in figure 17 (b) and (d).

$$\mu - \sigma < \text{ delay difference } < \mu + \sigma \tag{4.3}$$

This procedure was done for the PMT and the SiPMs separately. Only events which fulfil the condition in the PMT and the SiPMs were selected. For the time stamp of each peak in the SiPM array, first the SiPMs which measured the event had to be identified, then the average of the time positions of all SiPMs which measured the event was taken. The time delay cut was performed for all datasets separately.

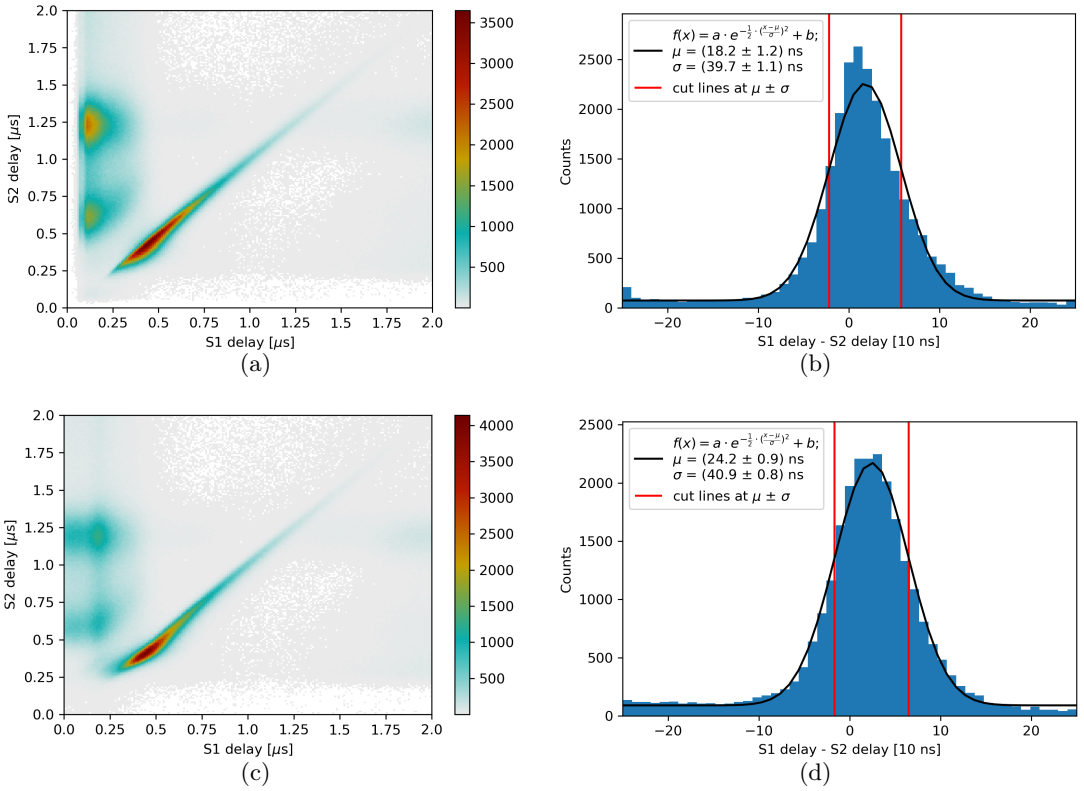

Figure 17: (a), (c): The events of all datasets in the S1 delay-S2 delay plane for the PMT and the SiPMs. As expected, the krypton events lie on the diagonal. (b), (d): Illustration of the time delay cut in the PMT and the SiPMs respectively. The cut lines are marked in red. The plots are from dataset 190202_1101.

Time constant

As a cross-check of the data, the half life $T_{1/2}$ of the intermediate state can be calculated after the time delay cut is performed. To do so, the S1 and S2 delays in the PMT as well as in the SiPMs were histogrammed and fitted with an exponential function, as illustrated in figure 18 (a)-(d). The fit directly gives the decay rate λ as one of the free fitting variables of the function $N(t) = N_0 \cdot e^{-\lambda \cdot t}$. The half life as well as the time constant can then easily be calculated from λ through $T_{1/2} = \frac{\ln(2)}{\lambda} = \tau \cdot \ln(2)$. Like this, four values of $T_{1/2}$ were obtained for each dataset. Finally the average values of all datasets were calculated. The best result was obtained for the S1 delay in the PMT, where

$$T_{1/2} = (163 \pm 7)\,\text{ns}. \tag{4.4}$$

This result is in agreement with the literature value of $T_{1/2} = (156.8 \pm 0.5)\,\text{ns}$ [56]. The result for the S1 delay in the SiPMs was $T_{1/2} = (167 \pm 7)\,\text{ns}$.

Error estimation: The error on the number of entries N in a bin of the histogram was assumed to be $\sigma_N = \sqrt{N}$. The errors on the fit parameters were then obtained, by diagonalizing and taking the square root of the Jacobian matrix, returned from the fitting tool (scipy.optimize.curve_fit), which uses the least square algorithm. The error on $T_{1/2}$ for each dataset, also shown in figure 18, was then simply calculated by Gaussian error propagation from λ. For the final result, the average of $T_{1/2}$ for all datasets, the error was estimated as their standard deviation.

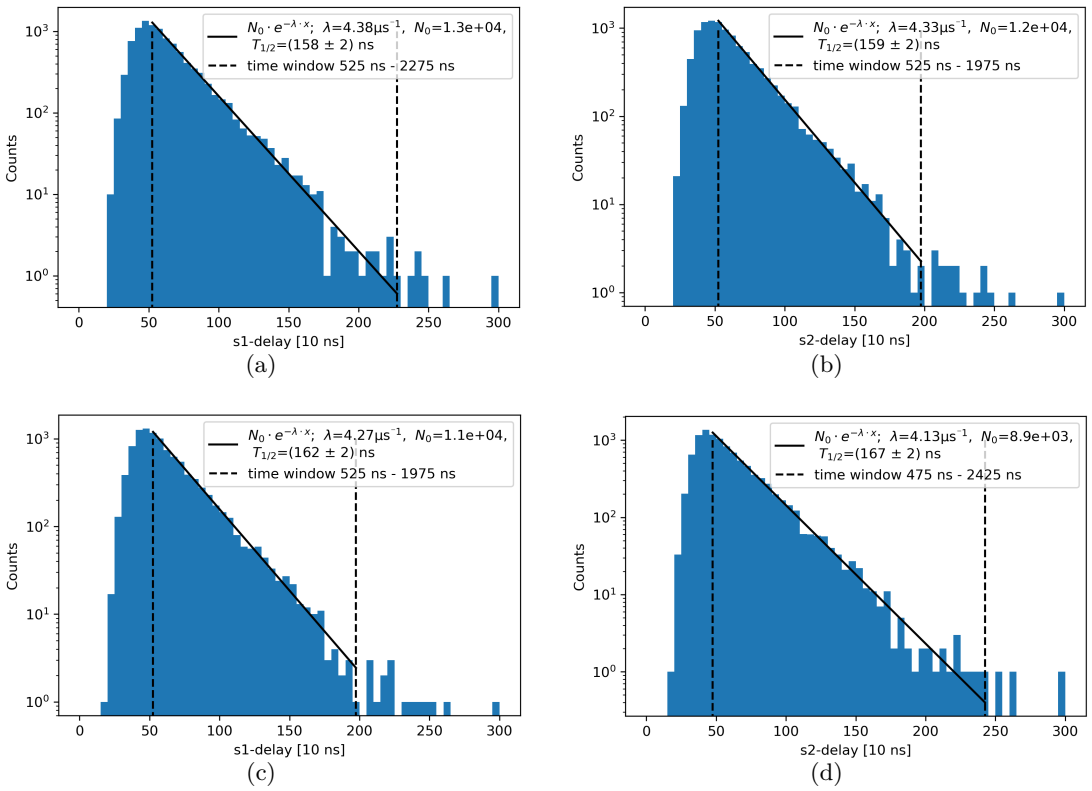

Figure 18: Fit of the time constant to the histogrammed delay. (a): S1 signal PMT, (b): S2 signal PMT, (c): S1 signal SiPMs, (d): S2 signal SiPMs. The plots are from the dataset 190202_1101.

4.4.2 S2 width cut

The S2 width cut is mainly needed to cut gas events and accidental coincidences. For a typical event in the bulk of the detector, the S2 width raises for longer drifttimes because the drifting electrons disperse. Histogramming the S2 width against drifttime this behaviour can be observed.
To get the cut values in each vertical slice of the histogram the 2.3% and 97.7% percentiles were marked, represented by the blue dots in figure 19. Then, the percentiles with drifttimes corresponding to a z-position inside the bulk of the TPC were selected based on values from Francesco Piastra's PhD thesis, listed in table 3. The allowed region is marked by the black dashed lines in figure 19. A fit was then performed through the selected percentiles for two different fit functions. One is an empirical function that fits the datapoints very well. The obtained cut is then

$$a_0 + b_0 \cdot t + \sqrt{c_0 \cdot t} < \text{ S2 width } < a_1 + b_1 \cdot t + \sqrt{c_1 \cdot t}, \tag{4.5}$$

where a_i, b_i and c_i are the parameters of the fit and t is the drifttime. The cut can be seen in figure 19 (a). The second fit function, shown in figure 19 (b), comes from the diffusion model [60]. The diffusion model does not describe precisely the observed behaviour for the lowest and highest drifttimes, therefore the cut obtained from the empirical fit function was used for the following analysis.

The cut was performed for different voltages from $-0.6\,\text{keV}$ to $-3.0\,\text{keV}$ separately, because the S2 width as a function of drifttime depends on the drift velocity which directly depends on the applied drift voltage. An overview of the various drift fields that were used for the analysis can be found in table 4.

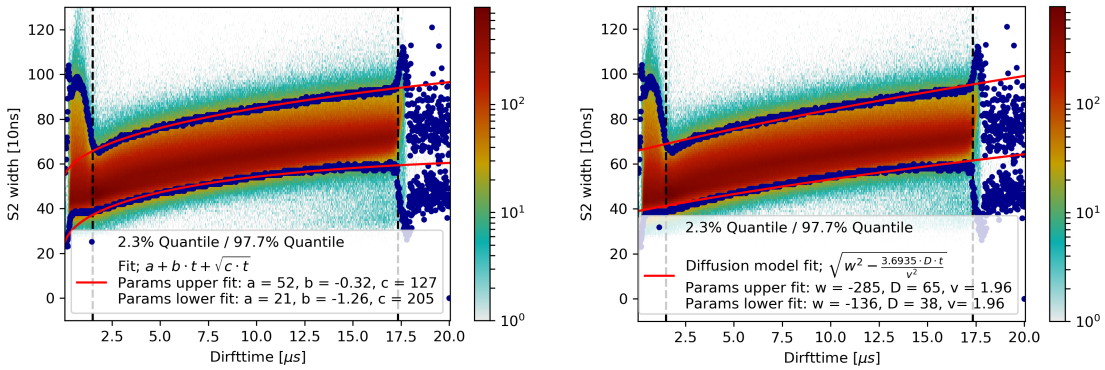

Figure 19: (a): S2 width cut with an empirical fit function. (b): S2 width cut with the diffusion model fit. The cut lines are marked in red. The plots are for the datasets with a drift field of 968 V/cm.

4.4.3 Fiducial volume cut

The fiducial volume cut is mainly applied in order to cut background events. A significant part of the background events take place in the gas phase (gas events) or come from decays in the TPC walls (wall events).
An accurate position reconstruction is only possible in the middle of the detector because of the geometry of the SiPM array. Therefore, the fiducial volume cut selects events only in the middle of the detector, where the position reconstruction is good and where it is very unlikely that an event comes from the wall. The outermost knot of the mesh which is clearly locatable, at $r = 9.7\,\mathrm{mm}$, was shown in figure 15 (a). Consequently, this value was taken as the outer boundary of the fiducial volume cut in the x-y plane:

$$0\,\mathrm{mm} < r < 9.7\,\mathrm{mm} \tag{4.6}$$

The fiducial volume cut also selects in z-direction. Not only events from the gas phase or outside the detector volume are cut away, but also events which took place in the high electric field region near the cathode and gate [4]. The selected z region was

$$-25\,\mathrm{mm} < z < -5\,\mathrm{mm}. \tag{4.7}$$

The cut lines are marked in red in figure 26. The fiducial volume cut was done in the same way for all datasets. It selects 25% of the TPC volume which contains about 17 g of liquid xenon.

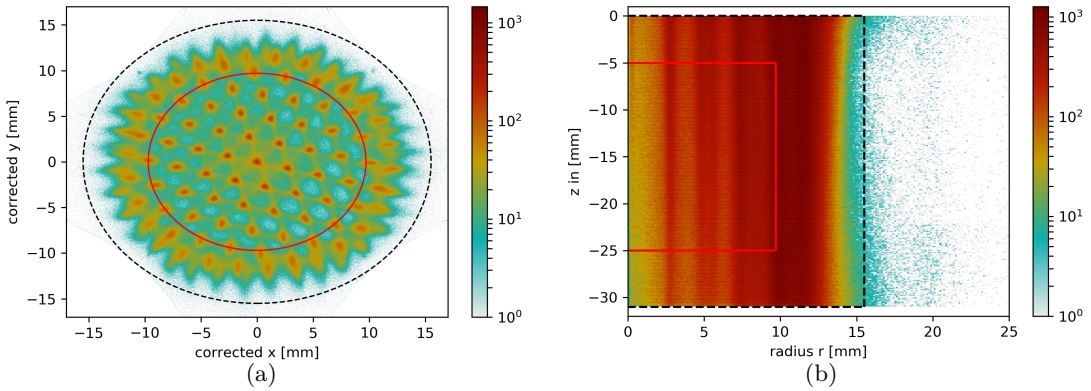

(a) (b)

Figure 20: Fiducial volume cut from (a): top and (b): side view. The cut line is marked in red while the TPC wall is marked by the black dashed line. The plots contain the events of all datasets.

4.4.4 S2 area fraction top cut

The S2 area fraction top cut is mainly needed to cut gas events, which typically have a large area fraction in the top array. The reason for this is that the gas phase is on the top, thus the SiPMs cover a larger solid angle than the PMT for those events. Histogramming the area fraction in the top array against the total area shows a clear population of events and only few gas events. This can be observed in figure 21.
To get the cut lines, an interval around the average area fraction top was selected such that no signal events are cut away:

$$0.21 < \text{ S2 area fraction top } < 0.31. \tag{4.8}$$

The cut was done the same way for all datasets.

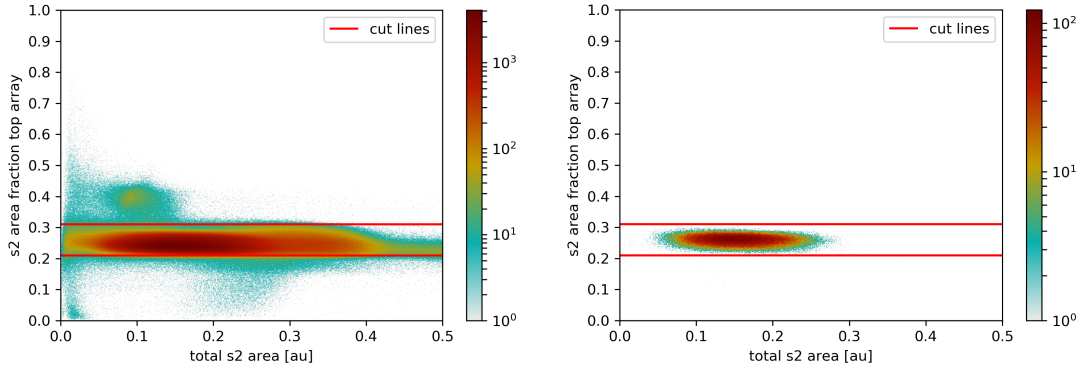

(a) (b)

Figure 21: Illustration of the area fraction top cut with (a): no cuts applied and (b): fiducial volume cut and time delay cut already applied. The cut lines are marked in red and the plots contain events of all datasets. While the cut efficiency of the area fraction top cut alone is 68% as mentioned in table 1, it cuts only very few events additionally to the fiducial volume cut and the time delay cut.

4.5 Corrections

Because of the geometry of the detector and the recombination of electrons with ions, the same type of event does not lead to the same signal size depending on where in the detector it took place. This effects needs to be corrected for in order to estimate the light yield of the detector.

4.5.1 Electron lifetime correction

A drifting electron in the TPC has a certain probability to recombine with ionized xenon atoms or impurities. The recombination probability is assumed to be constant throughout the detector. This results in an exponential decrease of the number of electrons with increasing drifttime. Analogous to the time constant in radioactive decays, the free electron lifetime is defined such that $N_{e^-}(t) = N_0 \cdot e^{-t/t_e}$ gives the number of electrons as a function of drifttime t, where t_e is the electron lifetime.
To get the correction, the S2 area was histogrammed against the drifttime. Then, in each slice of the histogram inside the detector volume, the 50% percentiles were marked, and an exponential fit through the data-points was performed. This can be seen in figure 22 (a). The area was then corrected like written in Eq. 4.9, by dividing it through the fit value at the given drifttime. To scale the result, the fit function value at zero drifttime was taken as a reference. The result can be seen in figure 22 (b).

$$S2 = N_0 \cdot \frac{S2(t)}{N_{e^-}(t)} \tag{4.9}$$

The values for the drifttime from gate/cathode to the anode as well as the drift velocity were taken from table 3 in the appendix.

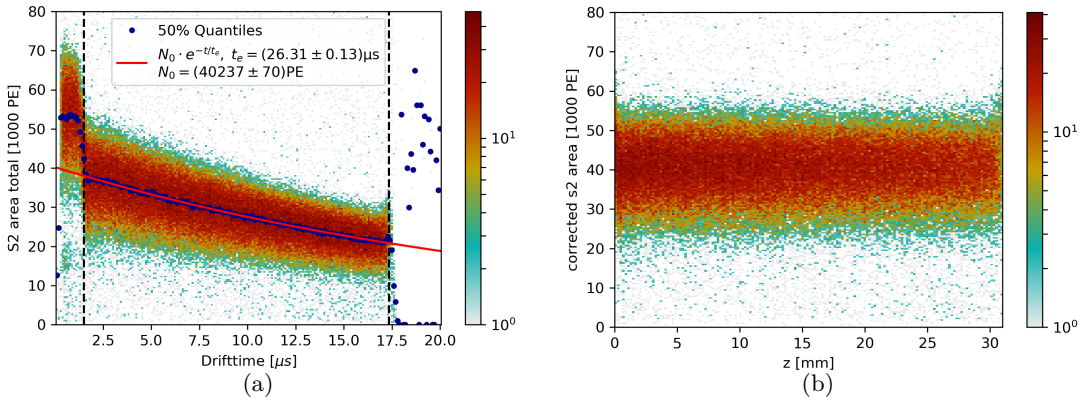

(a) (b)

Figure 22: (a): Fit to the decreasing uncorrected S2 area as a function of drifttime. (b): The corrected S2 area as a function of z. The plots are from the dataset 190202_1101.

The correction was done for all datasets separately, because the electron lifetime varied a lot between the different datasets. Values between $t_e = 8\,\mu s$ and $t_e = 72\,\mu s$ were reached. $8\,\mu s$ is about half of the maximal drifttime which means that for those events only one fourth of the electrons reach the gas phase. This is not a problem, because the S2 signal is, with about $40\,000\,PE$ at zero drifttime, large enough. The electron lifetime for all datasets can be seen in figure 23.

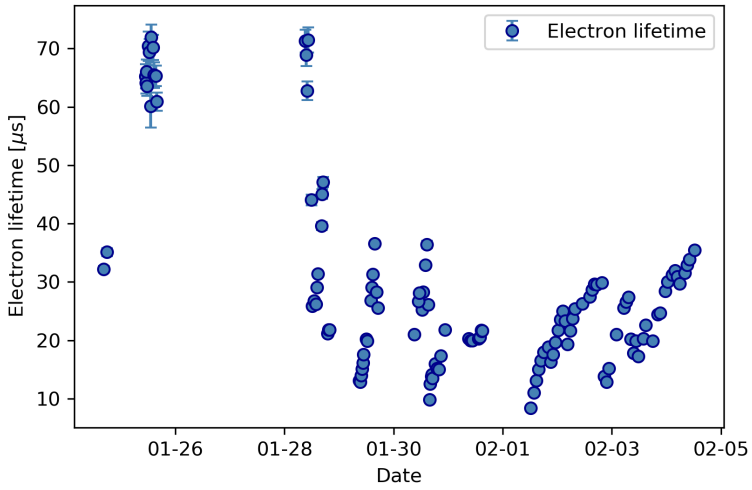

Figure 23: The electron lifetime of all datasets, plotted against the date at which it was taken. The average electron lifetime was $t_e = (29 \pm 16)\,\mu s$.

4.5.2 S1 area correction

The size of the S1 signals depends on the position of the event inside the TPC. The reason is the cylindrical geometry of the TPC, which leads to different solid angles covered by the PMT and the SiPM array depending on the position where the event took place. An event in the bottom part of the TPC leaves a stronger signal in the PMT than in the SiPMs on the top, and vice-versa. Plotting the S1 area in the PMT/SiPM against drifttime shows the expected behaviour as visible in figure 24 (a) and (c).
To get the correction, again the 50% percentiles were marked in the histogram and a fit was performed through the datapoints inside the TPC. To fit the number of photoelectrons as a function of the drifttime t, a fourth order polynomial was used:

$$N_\gamma(t) = a + b \cdot t + c \cdot t^2 + d \cdot t^3 + e \cdot t^4, \tag{4.10}$$

where a, b, c, d and e are the parameters to fit. The correction was then done analogous to the electron lifetime correction, but taking an event in the middle of the TPC as a

reference to scale the result:

$$S1 = N_\gamma(t_m) \cdot \frac{S1(t)}{N_\gamma(t)} \text{ where } t_m = \frac{t_{min} + t_{max}}{2}. \tag{4.11}$$

The values for t_{min} and t_{max} were again taken from table 3. The correction was done for the PMT and and the SiPMs separately, as well as for the six different applied drift voltages. This is necessary because the drifttime range to fit depends on the drift field. The results can be found in figure 24 (b) and (d).

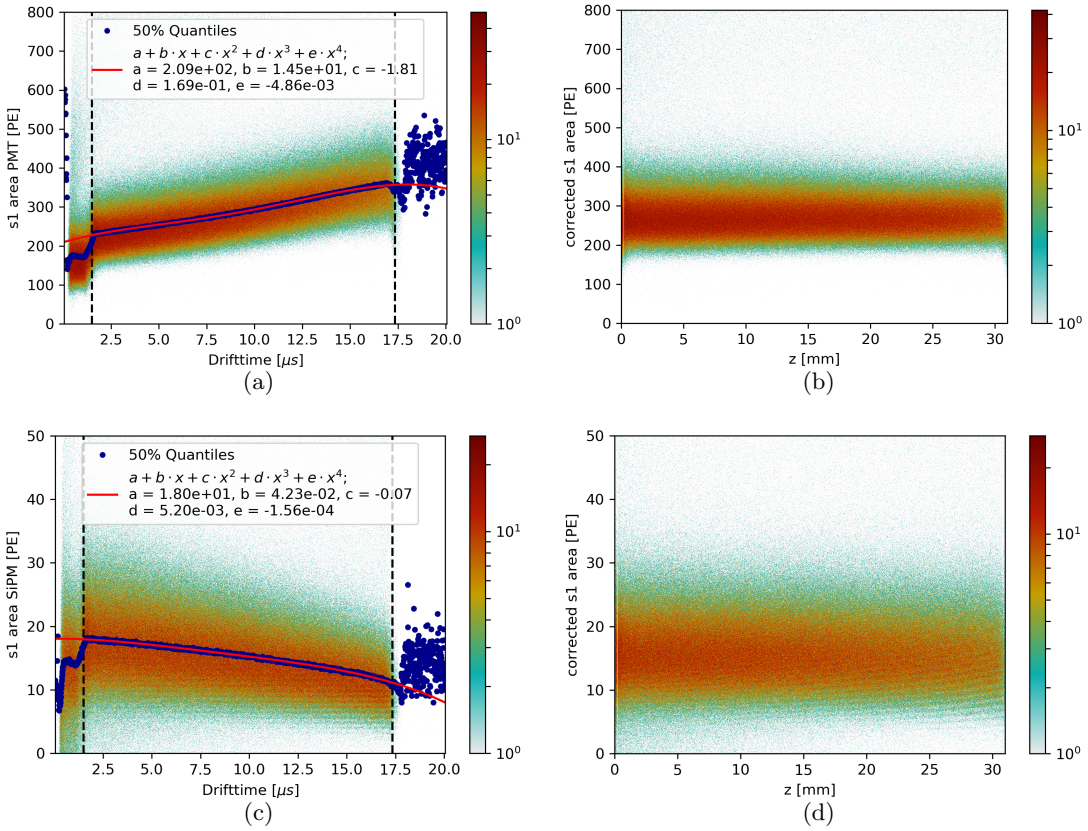

Figure 24: (a), (c): Fit to the uncorrected S1 area in the PMT and SiPMs as a function of drifttime. (b), (d): The corrected S1 area in the PMT and SiPMs as a function of z. All plots are for the datasets with a drift field of 968 V/cm.

4.6 Results

4.6.1 Light and charge yield

Plotting the corrected S1 area against the corrected S2 area and applying all the cuts to the data, a clear population of krypton events shows up. The charge/light anti-correlation can clearly be seen, as shown in figure 25. To calculate the light yield L_{S1} and charge yield Q_{S2}, the largest S1/S2 area of each event was first converted into units of photoelectrons (PE) by applying a conversion factor[2]. Then, the population was fitted with an ellipse (2d-Gaussian distribution) to extract the mean and the standard deviation. The yields were then calculated by simply dividing the mean area $S1/S2$ in units of photoelectrons by the well known energy E of the corresponding line. For the $E_1 = 32\,\text{keV}$ line at $-3\,\text{kV}$ cathode voltage, this lead to the following result:

$$L_{S1} = S1/E_1 = (6.2 \pm 1.0)\,\text{PE/keV} \tag{4.12}$$

$$Q_{S2} = S2/E_1 = (1050 \pm 200)\,\text{PE/keV} \tag{4.13}$$

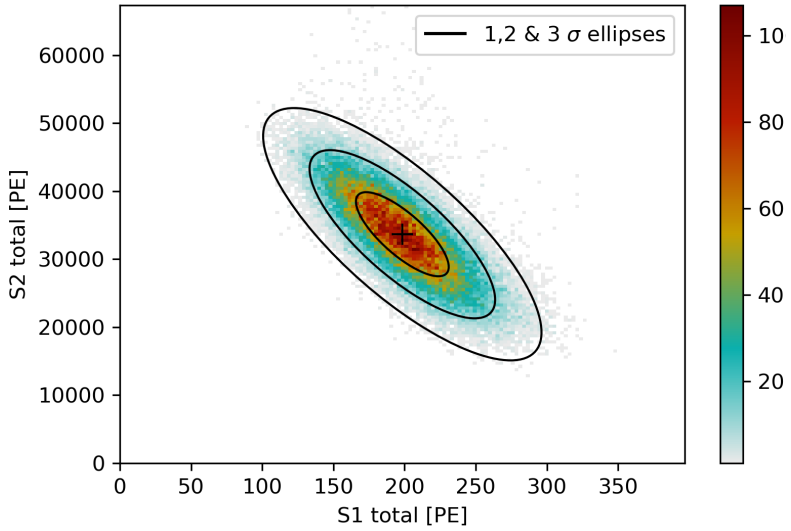

Figure 25: Light and charge yield of the 32 keV line at 968 V/cm drift field.

[2] A pixel in the waveform has a width of 10 ns and a hight of 2.75 µA, giving an area of 27.5 pC. The area in units of coulomb has further to be divided by the gain of the PMT/SiPM and the electron charge to get the number of photoelectrons.

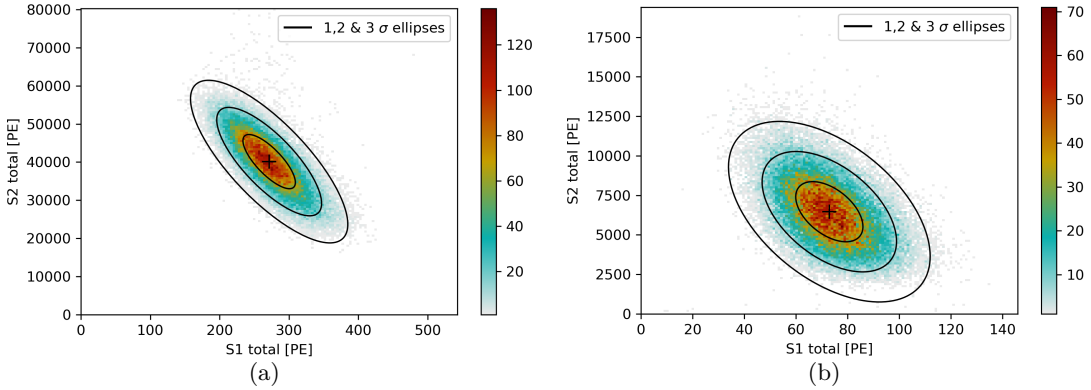

Figure 26: Light an charge yield of (a): the 41 keV line and (b): the 9.4 keV line. Both plots are at a drift field of 968 V/cm.

Error estimation: The error on the light and charge yield was calculated by taking one standard deviation of the S1/S2 area data points, corresponding to the innermost ellipse in figure 25, and converting it into units of PE/keV.

4.6.2 Estimation of $g1$ and $g2$

The detector response parameters $g1$ and $g2$ are defined as

$$g1 := S1/N_\gamma \text{ and } g2 := S2/N_{e^-}, \tag{4.14}$$

where $S1$ and $S2$ are the S1/S2 signal areas in units of PE, N_γ is the number of photons and N_{e^-} is the number of electrons produced in an event. Ideally, these response parameters do not depend on the source energy or the drift field.
The total deposited energy in the TPC is related to the number of produced photons and electrons through

$$E = (N_\gamma + N_{e^-}) \cdot W, \tag{4.15}$$

where $W = (13.7 \pm 0.2)$ eV is the mean energy needed to produce a photon or an electron in liquid xenon [53].
With these formulas, a combined energy scale can be derived. Solving Eq. 4.14 for N_γ and N_{e^-} and plugging it in Eq. 4.15 gives

$$E = \left(\frac{S1}{g1} + \frac{S2}{g2}\right) \cdot W. \tag{4.16}$$

Plotting the S1 light yield $L_{S1} = S1/E$ against the S2 charge yield $Q_{S2} = S2/E$ for different drift fields (Doke plot) as in figure 27, one clearly sees that all data points are located on a line. Performing a linear fit through the data points ($Q_{S2} = a \cdot L_{S1} + b$), one is now able to extrapolate the linear dependence down to $L_{S1} = 0$ where $Q_{S2} = b$.

At this point the first therm in 4.16 is zero and the equation can easily be solved for $g2$, giving $g2 = \frac{S2 \cdot W}{E} = Q_{S2}(L_{S1} = 0) \cdot W = b \cdot W$. In the exact same way, for $Q_{S2} = 0$ it can be found that $g1 = -\frac{b}{a} \cdot W$. Like this, the following values for $g1$ and $g2$ were found:

$$g1 = (0.150 \pm 0.009)\,\mathrm{PE}/\gamma \tag{4.17}$$

$$g2 = (32.7 \pm 1.1)\,\mathrm{PE}/\mathrm{e}^- \tag{4.18}$$

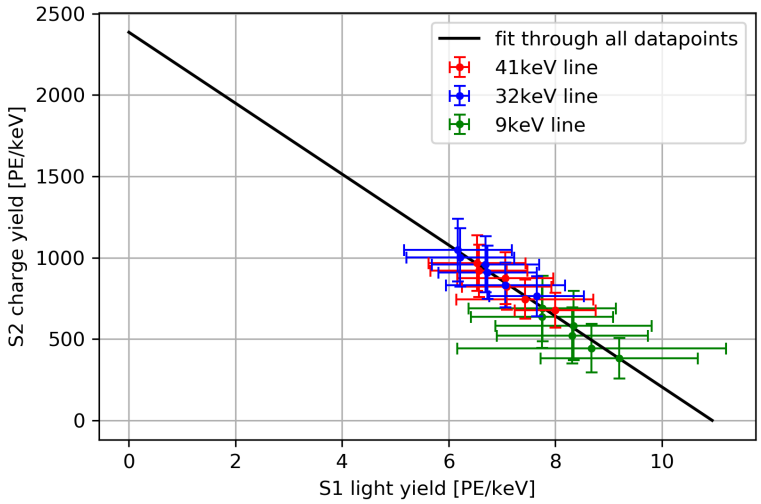

Figure 27: Linear fit to light and charge yields of all three lines at different drift fields. The data taken at higher drift voltages is shifted to the upper left compared to the data taken at lower drift voltages.

The response parameter $g2$ was also calculated for the S2 signal in the PMT/SiPMs only. The corresponding plots can be found in figures 30 and 31 (a)-(d) in the appendix. The following values were found:

$$g2_{\mathrm{PMT}} = (23.6 \pm 0.8)\,\mathrm{PE}/\mathrm{e}^- \tag{4.19}$$

$$g2_{\mathrm{SiPM}} = (9.1 \pm 0.3)\,\mathrm{PE}/\mathrm{e}^- \tag{4.20}$$

Error estimation: The error on a and b were taken from the fitting tool (scipy.odr.ODR) which uses orthogonal distance regression and takes into account errors in both directions on L_{S1} and Q_{S2}. The errors on $g1$ and $g2$ were then calculated by Gaussian error propagation from a, b and W.

5 Discussion and Conclusion

In an earlier stage of Xurich, the detector operated with two PMTs, one on the top and one on the bottom, while the other parts of the setup remained widely the same. Therefore, comparing the result of Xurich II with SiPMs to the results achieved before the upgrade, the performance of the PMT and SiPMs can be directly compared. Since the S2 signals of the 41 keV line in the top PMT saturated the ADC before the upgrade, the analysis was done with the S2 signal in the bottom PMT only. The resulting Doke plots before and after the upgrade can be seen in figure 28.

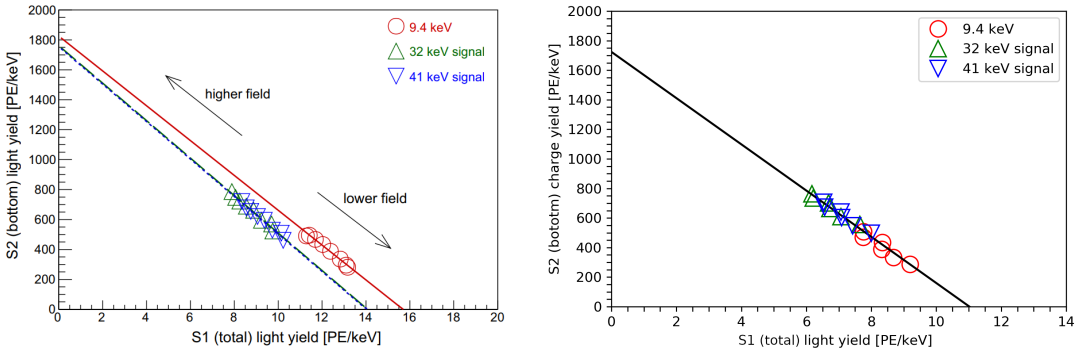

Figure 28: Comparison of the Doke plots (a): before and (b): after the setup modification. Figure (a) from [53].

The main difference between the two plots is that for the upgraded Xurich II all datapoints lay on one line as theoretically expected. The results for the detector response parameters $g1$ and $g2_{\mathrm{PMT}}$, with S2 in the bottom PMT only, before the upgrade as well as the corresponding parameters afterwards[1] are listed in table 2.

Parameter	**Before upgrade**	**After upgrade**
$\boldsymbol{g1}$	$(0.191 \pm 0.006)\,\mathrm{PE}/\gamma$	$(0.151 \pm 0.008)\,\mathrm{PE}/\gamma$
$\boldsymbol{g2_{\mathrm{PMT}}}$	$(24.4 \pm 0.4)\,\mathrm{PE}/\mathrm{e}^-$	$(23.6 \pm 0.8)\,\mathrm{PE}/\mathrm{e}^-$

Table 2: Comparison of the detector response parameters. The values before the upgrade are from [53].

[1]The parameter $g1$ is not exactly the same as in Eq. 4.17 because performing the fit on the S2 bottom charge yield, the x-axis intersection point changed, even though the S1 light yields are exactly the same.

The response parameter $g1$ as well as all light yields slightly decreased for Xurich II with SiPMs. This can be explained by the lower light detection efficiency of the SiPMs compared to the PMT. The parameters $g2_{\mathrm{PMT}}$ before and after the upgrade are compatible within the error. This is expected because the S2 bottom charge yield was measured with the same PMT in both experiments.
In figure 29 the ellipse of the 32 keV line with a drift field of 968 V/cm before and after the installation of the top SiPM array can be compared. The ellipse of Xurich II with SiPMs has a much clearer population. This is mainly due to the position reconstruction in the x-y plane, which allows to cut events at the edge of the detector in the fiducial volume cut. These events typically have a much lower charge collection and are therefore located below the ellipse.

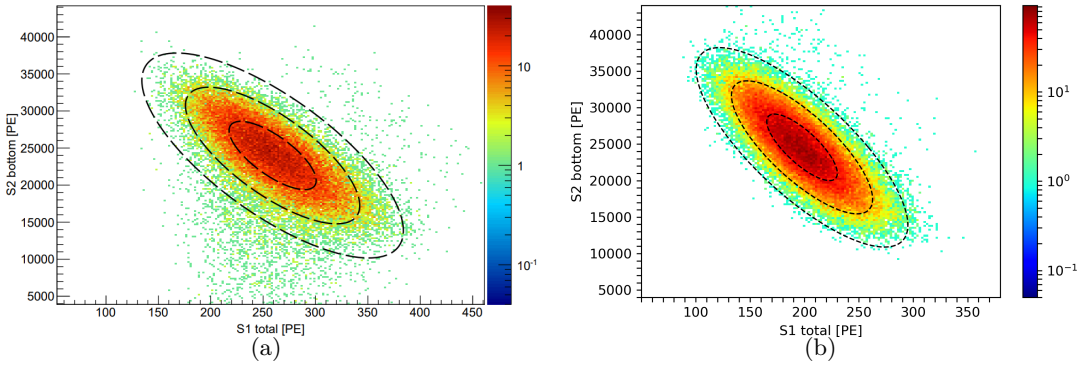

Figure 29: Comparison of the ellipse of the 32 keV line with a drift field of 968 V/cm. (a): Before and (b): after the set up modification. Figure (a) from [53].

As this comparison shows, the main advantage of the SiPMs for Xurich is their small size which allows for a good position reconstruction and helps to reduce background through the fiducial volume cut. However, for larger detectors a good position reconstruction can also be achieved with PMTs. The main advantage of the SiPMs for large detectors is their low radioactivity. Nevertheless, based on this comparison one can conclude that the SiPMs work very well and are indeed a promising candidate for photosensors in future experiments, especially if their dark count rate can be further reduced.
For the future, a next upgrade of Xurich II is planned, in which also the bottom PMT will be substituted by a SiPM array, to test the pre-amplifier board and the behaviour of the SiPMs in the cold liquid phase.

6 Appendix

Drift field [$\frac{V}{cm}$]	Gate time t_{min} [µs]	Cathode time t_{max} [µs]	Drift velocity [$\frac{mm}{µs}$]
220 ± 30	1.8 ± 0.1	20.85 ± 0.03	1.63 ± 0.01
260 ± 30	1.8 ± 0.1	20.64 ± 0.05	1.64 ± 0.01
380 ± 30	1.7 ± 0.1	19.91 ± 0.05	1.70 ± 0.01
530 ± 30	1.6 ± 0.1	18.96 ± 0.05	1.79 ± 0.02
670 ± 20	1.6 ± 0.1	18.35 ± 0.05	1.85 ± 0.01
820 ± 20	1.6 ± 0.1	17.79 ± 0.07	1.91 ± 0.02
960 ± 30	1.5 ± 0.1	17.34 ± 0.05	1.96 ± 0.02
1260 ± 30	1.5 ± 0.1	16.98 ± 0.09	2.00 ± 0.02

Table 3: Table of drifttimes and drift velocities at different fields. Table taken from [58].

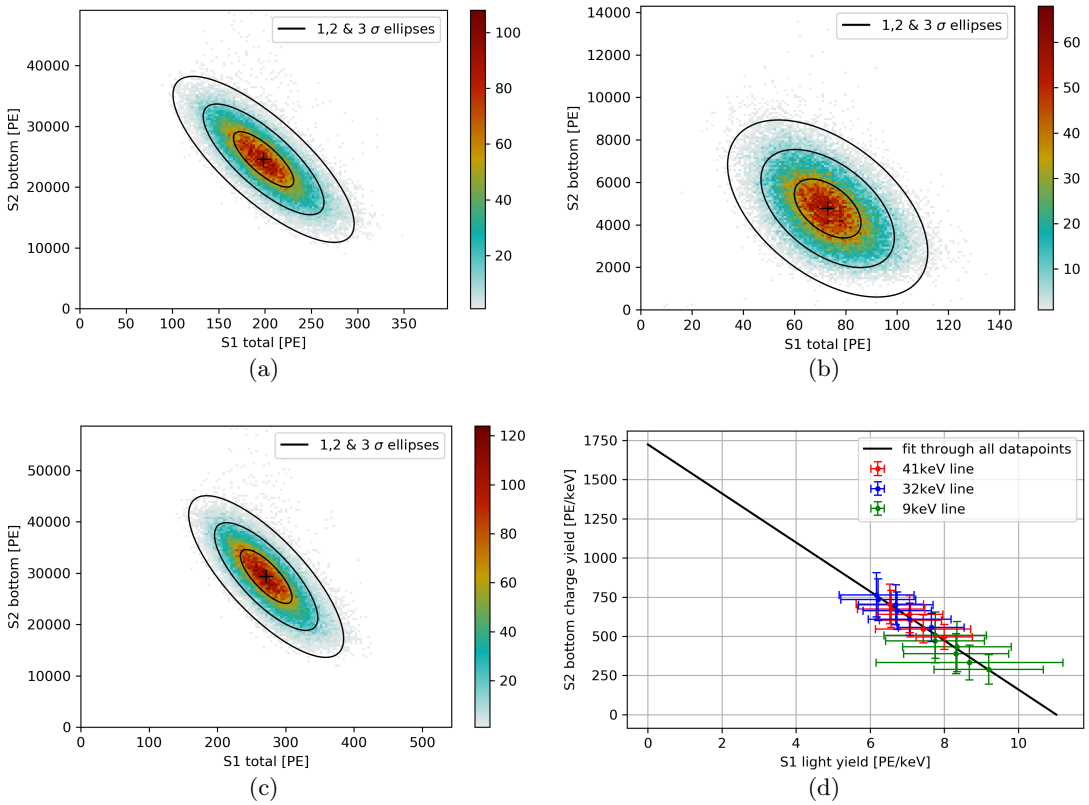

Figure 30: Light an charge yield of (a): the 32 keV line, (b): the 9.4 keV line and (c): the 41 keV line at a drift field of 968 V/cm and using the S2 signal in the PMT only. Figure (d) shows the corresponding Doke plot.

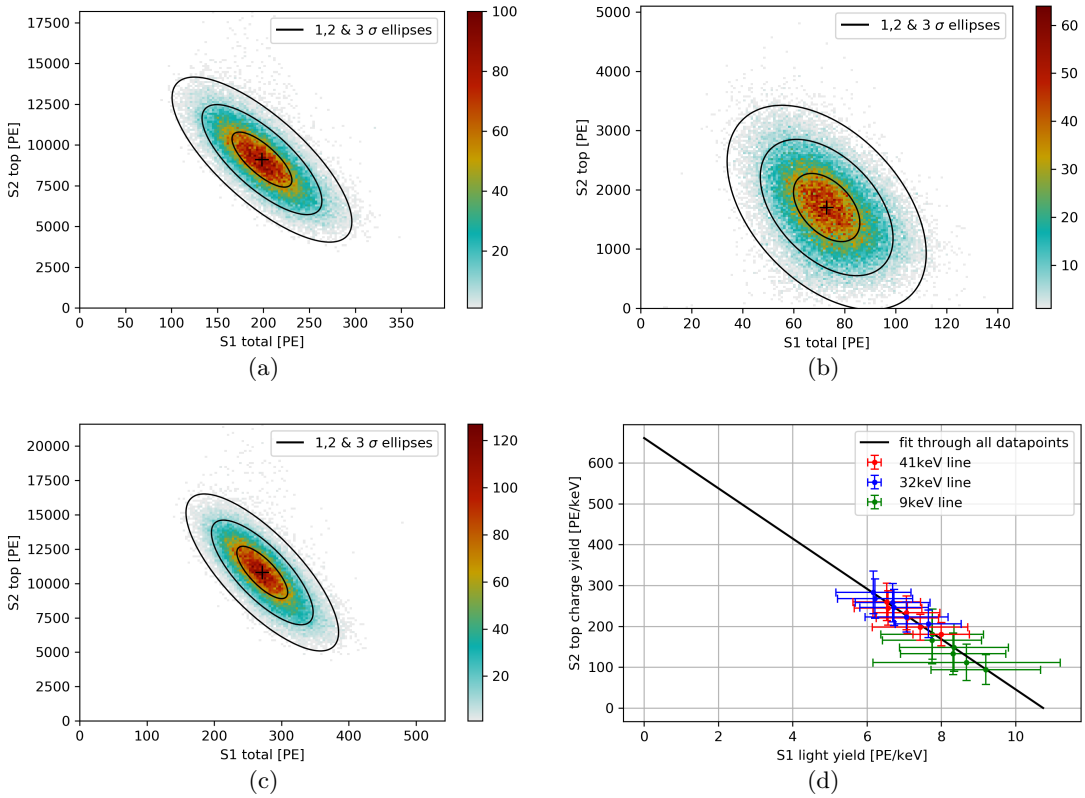

Figure 31: Light an charge yield of (a): the 32 keV line, (b): the 9.4 keV line and (c): the 41 keV line at a drift field of 968 V/cm and using the S2 signal in the SiPMs only. Figure (d) shows the corresponding Doke plot.

Drift field [$\frac{\text{V}}{\text{cm}}$]	**Cathode voltage** [kV]	**Datasets**	**Statistics**
968	-3.0	85	27 482 799
806	-2.5	8	400 000
645	-2.0	8	400 000
484	-1.5	8	400 000
323	-1.0	6	300 000
194	-0.6	3	150 000

Table 4: Table of the available data at different drift fields, used for the Doke plot.

Filename	Cathode Voltage [kV]	Statistics	ZLE	Misalignment
190124_1631	-3.0	50 000	No	no
190124_1645	-3.0	14 109	No	yes
190124_1653	-3.0	50 000	No	yes
190124_1707	-3.0	50 000	No	yes
190124_1721	-3.0	50 000	No	yes
190124_1735	-3.0	50 000	No	yes
190124_1749	-3.0	31 799	No	no
190125_1049	-3.0	50 000	No	no
190125_1102	-3.0	50 000	No	no
190125_1116	-3.0	50 000	No	no
190125_1130	-3.0	50 000	No	no
190125_1144	-3.0	50 000	No	yes
190125_1158	-3.0	50 000	No	yes
190125_1212	-3.0	50 000	No	no
190125_1226	-3.0	50 000	No	no
190125_1240	-3.0	50 000	No	yes
190125_1254	-3.0	50 000	No	yes
190125_1308	-3.0	50 000	No	no
190125_1322	-3.0	50 000	No	no
190125_1410	-3.0	50 000	No	no
190125_1434	-3.0	50 000	No	no
190125_1458	-3.0	50 000	No	yes
190125_1521	-3.0	50 000	No	no
190128_0906	-2.5	50 000	No	no
190128_0930	-2.5	50 000	No	no
190128_0953	-2.5	50 000	No	no
190128_1016	-2.5	50 000	No	no
190128_1039	-2.5	50 000	No	yes
190128_1103	-2.5	50 000	No	yes
190128_1126	-2.5	50 000	No	yes
190128_1150	-2.5	50 000	No	no
190128_1215	-2.5	50 000	No	no
190128_1238	-2.5	50 000	No	yes
190128_1301	-2.5	50 000	No	no
190128_1325	-2.5	50 000	No	yes
190128_1349	-2.5	50 000	No	no
190128_1414	-2.0	50 000	No	no
190128_1438	-2.0	50 000	No	no
190128_1502	-2.0	50 000	No	yes
190128_1612	-2.0	50 000	No	no
190128_1636	-2.0	50 000	No	no
190128_1700	-2.0	50 000	No	no
190128_1723	-2.0	50 000	No	yes
190128_1747	-2.0	50 000	No	yes
190128_1810	-2.0	50 000	No	yes
190128_1833	-2.0	50 000	No	yes
190128_1855	-2.0	50 000	No	no

190128_1918	-2.0	50 000	No	no
190128_1941	-2.0	50 000	No	no
190129_0855	-1.5	50 000	No	no
190129_0917	-1.5	50 000	No	no
190129_0940	-1.5	50 000	No	no
190129_1003	-1.5	50 000	No	no
190129_1026	-1.5	50 000	No	no
190129_1049	-1.5	50 000	No	no
190129_1112	-1.5	50 000	No	yes
190129_1135	-1.5	50 000	No	yes
190129_1158	-1.5	50 000	No	no
190129_1222	-1.5	50 000	No	no
190129_1402	-1.0	50 000	No	no
190129_1426	-1.0	50 000	No	no
190129_1450	-1.0	50 000	No	no
190129_1514	-1.0	50 000	No	yes
190129_1538	-1.0	50 000	No	no
190129_1601	-1.0	50 000	No	yes
190129_1624	-1.0	50 000	No	no
190129_1648	-1.0	50 000	No	yes
190129_1711	-1.0	50 000	No	no
190129_1735	-1.0	50 000	No	yes
190130_0904	-0.6	50 000	No	no
190130_1013	-0.6	50 000	No	yes
190130_1036	-0.6	50 000	No	yes
190130_1100	-0.6	50 000	No	no
190130_1123	-0.6	50 000	No	no
190130_1239	-3.0	50 000	No	no
190130_1302	-3.0	50 000	No	no
190130_1340	-3.0	50 000	No	yes
190130_1354	-3.0	50 000	No	no
190130_1408	-3.0	50 000	No	yes
190130_1423	-3.0	50 000	No	yes
190130_1438	-3.0	50 000	No	no
190130_1453	-3.0	50 000	No	yes
190130_1508	-3.0	50 000	No	no
190130_1523	-3.0	50 000	No	yes
190130_1551	-3.0	50 000	No	no
190130_1606	-3.0	50 000	No	no
190130_1621	-3.0	50 000	No	yes
190130_1621	-3.0	50 000	No	yes
190130_1636	-3.0	50 000	No	no
190130_1650	-3.0	50 000	No	no
190130_1704	-3.0	50 000	No	no
190130_1719	-3.0	200 000	No	yes
190130_1811	-3.0	200 000	No	no
190130_1903	-3.0	200 000	No	no
190130_1955	-3.0	200 000	No	no
190130_2047	-3.0	200 000	No	no

190130_2233	-3.0	200 000	No	no
190131_0902	-3.0	200 000	No	no
190131_0954	-3.0	200 000	No	no
190131_1046	-3.0	200 000	No	no
190131_1207	-3.0	200 000	No	yes
190131_1259	-3.0	200 000	No	yes
190131_1326	-3.0	50 000	No	no
190131_1341	-3.0	50 000	No	no
190131_1357	-3.0	50 000	No	no
190131_1428	-3.0	50 000	No	no
190131_1458	-3.0	50 000	No	no
190201_1212	-3.0	500 000	Yes	no
190201_1341	-3.0	500 000	Yes	no
190201_1445	-3.0	500 000	Yes	no
190201_1548	-3.0	500 000	Yes	no
190201_1652	-3.0	500 000	Yes	no
190201_1755	-3.0	500 000	Yes	no
190201_1858	-3.0	500 000	Yes	yes
190201_2002	-3.0	500 000	Yes	no
190201_2106	-3.0	500 000	Yes	no
190201_2210	-3.0	500 000	Yes	no
190201_2313	-3.0	500 000	Yes	no
190202_0017	-3.0	500 000	Yes	no
190202_0120	-3.0	500 000	Yes	no
190202_0224	-3.0	500 000	Yes	no
190202_0328	-3.0	500 000	Yes	no
190202_0432	-3.0	500 000	Yes	no
190202_0536	-3.0	500 000	Yes	no
190202_0640	-3.0	500 000	Yes	no
190202_0749	-3.0	500 000	Yes	no
190202_0853	-3.0	500 000	Yes	yes
190202_0957	-3.0	500 000	Yes	yes
190202_1101	-3.0	500 000	Yes	no
190202_1205	-3.0	500 000	Yes	yes
190202_1310	-3.0	500 000	Yes	yes
190202_1414	-3.0	500 000	Yes	no
190202_1622	-3.0	500 000	Yes	no
190202_1726	-3.0	500 000	Yes	no
190202_1830	-3.0	500 000	Yes	yes
190202_1934	-3.0	500 000	Yes	no
190202_2038	-3.0	500 000	Yes	no
190202_2141	-3.0	500 000	Yes	no
190202_2245	-3.0	500 000	Yes	no
190202_2348	-3.0	500 000	Yes	yes
190203_0056	-3.0	500 000	Yes	yes
190203_0200	-3.0	500 000	Yes	no
190203_0304	-3.0	500 000	Yes	yes
190203_0408	-3.0	500 000	Yes	yes
190203_0512	-3.0	500 000	Yes	no

190203_0616	-3.0	500 000	Yes	no
190203_0720	-3.0	500 000	Yes	no
190203_0825	-3.0	500 000	Yes	no
190203_0928	-3.0	500 000	Yes	no
190203_1032	-3.0	500 000	Yes	no
190203_1136	-3.0	500 000	Yes	no
190203_1240	-3.0	500 000	Yes	yes
190203_1345	-3.0	500 000	Yes	no
190203_1449	-3.0	500 000	Yes	no
190203_1553	-3.0	500 000	Yes	yes
190203_1657	-3.0	500 000	Yes	yes
190203_1802	-3.0	500 000	Yes	no
190203_1906	-3.0	500 000	Yes	yes
190203_2010	-3.0	500 000	Yes	no
190203_2115	-3.0	500 000	Yes	no
190203_2219	-3.0	500 000	Yes	yes
190203_2323	-3.0	500 000	Yes	no
190204_0027	-3.0	500 000	Yes	no
190204_0132	-3.0	500 000	Yes	yes
190204_0237	-3.0	500 000	Yes	no
190204_0341	-3.0	500 000	Yes	no
190204_0446	-3.0	500 000	Yes	no
190204_0550	-3.0	500 000	Yes	no
190204_0655	-3.0	500 000	Yes	yes
190204_0759	-3.0	500 000	Yes	no
190204_0904	-3.0	500 000	Yes	no
190204_1008	-3.0	500 000	Yes	no
190204_1113	-3.0	500 000	Yes	yes
190204_1218	-3.0	500 000	Yes	no

Table 5: Table of all analysed datasets from Xurich II with SiPMs Run2. ZLE stands for Zero Length Encoding and is a data acquisition mode, in which the waveforms are only saved, if a certain threshold is exceeded within the sample.

Bibliography

[1] Fritz Zwicky. "Die rotverschiebung von extragalaktischen nebeln". In: *Helvetica Physica Acta* 6 (1933), pp. 110–127.

[2] Laura Baudis. "The Search for Dark Matter". In: *European Review* 26.1 (2018), 70–81. DOI: 10.1017/S1062798717000783.

[3] L. Baudis et al. "Characterisation of Silicon Photomultipliers for liquid xenon detectors". In: *Journal of Instrumentation* 13.10 (2018), P10022–P10022. DOI: 10.1088/1748-0221/13/10/p10022. URL: https://doi.org/10.1088%2F1748-0221%2F13%2F10%2Fp10022.

[4] Julien Wulf. "Direct Dark Matter Search with XENON1T and Developments for Multi-ton Liquid Xenon Detectors". PhD thesis. Universität Zürich, 2018.

[5] J Aalbers et al. "DARWIN: towards the ultimate dark matter detector". In: *Journal of Cosmology and Astroparticle Physics* 2016.11 (2016), p. 017.

[6] Prasenjit Saha and Paul Taylor. "The Virial Theorem". In: *The Astronomers' Magic Envelope*. 2018.

[7] Prasenjit Saha and Paul Taylor. "Medium and Low-Mass Stars". In: *The Astronomers' Magic Envelope*. 2018.

[8] Vera C Rubin and W Kent Ford Jr. "Rotation of the Andromeda nebula from a spectroscopic survey of emission regions". In: *The Astrophysical Journal* 159 (1970), p. 379.

[9] KG Begeman, AH Broeils, and RH Sanders. "Extended rotation curves of spiral galaxies: Dark haloes and modified dynamics". In: *Monthly Notices of the Royal Astronomical Society* 249.3 (1991), pp. 523–537.

[10] Prasenjit Saha and Paul Taylor. "Gravitational Lensing". In: *The Astronomers' Magic Envelope*. 2018.

[11] Douglas Clowe et al. "A direct empirical proof of the existence of dark matter". In: *The Astrophysical Journal Letters* 648.2 (2006), p. L109.

[12] George F Smoot. "COBE observations and results". In: *AIP Conference Proceedings CONF-981098*. Vol. 476. 1. AIP. 1999, pp. 1–10.

[13] C. L. Bennett et al. "NINE-YEARWILKINSON MICROWAVE ANISOTROPY PROBE(WMAP) OBSERVATIONS: FINAL MAPS AND RESULTS". In: *The Astrophysical Journal Supplement Series* 208.2 (2013), p. 20. DOI: 10.1088/0067-0049/208/2/20. URL: https://doi.org/10.1088%2F0067-0049%2F208%2F2%2F20.

[14] Peter AR Ade et al. "Planck 2013 results. I. Overview of products and scientific results". In: *Astronomy & Astrophysics* 571 (2014), A1.

[15] Peter AR Ade et al. "Planck 2013 results. XXII. Constraints on inflation". In: *Astronomy & Astrophysics* 571 (2014), A22.

[16] Prasenjit Saha and Paul Taylor. "The Expanding Universe". In: *The Astronomers' Magic Envelope*. 2018.

[17] Prasenjit Saha and Paul Taylor. "The Cosmic Microwave Background". In: *The Astronomers' Magic Envelope*. 2018.

[18] Uroš Seljak, Anže Slosar, and Patrick McDonald. "Cosmological parameters from combining the Lyman-α forest with CMB, galaxy clustering and SN constraints". In: *Journal of Cosmology and Astroparticle Physics* 2006.10 (2006), p. 014.

[19] Carlos S Frenk and Simon DM White. "Dark matter and cosmic structure". In: *Annalen der Physik* 524.9-10 (2012), pp. 507–534.

[20] Alexander Kish. "Dark Matter Search with the XENON100 Experiment". PhD thesis. Universität Zürich, 2011.

[21] J Buckley et al. "Cosmic Frontier indirect dark matter detection working group summary". In: *arXiv preprint arXiv:1310.7040* (2013).

[22] M Ackermann et al. "Searching for dark matter annihilation from Milky Way dwarf spheroidal galaxies with six years of Fermi Large Area Telescope data". In: *Physical Review Letters* 115.23 (2015), p. 231301.

[23] Mark Thomson. *Modern particle physics*. Cambridge University Press, 2013.

[24] RCG Chaves et al. "The HESS galactic plane survey". In: *AIP Conference Proceedings*. Vol. 1085. 1. AIP. 2008, pp. 219–222.

[25] Max L Ahnen et al. "Indirect dark matter searches in the dwarf satellite galaxy Ursa Major II with the MAGIC Telescopes". In: *Journal of Cosmology and Astroparticle Physics* 2018.03 (2018), p. 009.

[26] J Holder et al. "Status of the VERITAS Observatory". In: *AIP Conference Proceedings*. Vol. 1085. 1. AIP. 2008, pp. 657–660.

[27] M Actis et al. "Design concepts for the Cherenkov Telescope Array CTA: an advanced facility for ground-based high-energy gamma-ray astronomy". In: *Experimental Astronomy* 32.3 (2011), pp. 193–316.

[28] S Desai et al. "Search for dark matter WIMPs using upward through-going muons in Super-Kamiokande". In: *Physical Review D* 70.8 (2004), p. 083523.

[29] Brian Feldstein et al. "Neutrinos at IceCube from heavy decaying dark matter". In: *Physical Review D* 88.1 (2013), p. 015004.

[30] V Barger et al. "PAMELA and dark matter". In: *Physics Letters B* 672.2 (2009), pp. 141–146.

[31] M Aguilar et al. "Electron and Positron Fluxes in Primary Cosmic Rays Measured with the Alpha Magnetic Spectrometer on the International Space Station". In: *Phys. Rev. Lett.* 113 (2014), p. 121102. DOI: 10.1103/PhysRevLett.113.121102. URL: http://cds.cern.ch/record/1756487.

[32] C. Corti et al. "SOLAR MODULATION OF THE LOCAL INTERSTELLAR SPECTRUM WITHVOYAGER 1, AMS-02,PAMELA, ANDBESS". In: *The Astrophysical Journal* 829.1 (2016), p. 8. DOI: 10.3847/0004-637x/829/1/8. URL: https://doi.org/10.3847%2F0004-637x%2F829%2F1%2F8.

[33] Patrick J Fox et al. "Missing energy signatures of dark matter at the LHC". In: *Physical Review D* 85.5 (2012), p. 056011.

[34] Craig E Aalseth et al. "CoGeNT: A search for low-mass dark matter using p-type point contact germanium detectors". In: *Physical Review D* 88.1 (2013), p. 012002.

[35] Ke-Jun Kang et al. "Introduction to the CDEX experiment". In: *Frontiers of Physics* 8.4 (2013), pp. 412–437. ISSN: 2095-0470. DOI: 10.1007/s11467-013-0349-1. URL: https://doi.org/10.1007/s11467-013-0349-1.

[36] R Agnese et al. "Search for low-mass weakly interacting massive particles with SuperCDMS". In: *Physical review letters* 112.24 (2014), p. 241302.

[37] Alain Benoit et al. "Improved exclusion limits from the EDELWEISS WIMP search". In: *Physics Letters B* 545.1-2 (2002), pp. 43–49.

[38] M Barnabe-Heider et al. "Improved spin-dependent limits from the PICASSO dark matter search experiment". In: *Physics Letters B* 624.3-4 (2005), pp. 186–194.

[39] C Amole et al. "Dark Matter Search Results from the PICO- 60 C 3 F 8 Bubble Chamber". In: *Physical review letters* 118.25 (2017), p. 251301.

[40] M Felizardo et al. "Final analysis and results of the phase II SIMPLE dark matter search". In: *Physical review letters* 108.20 (2012), p. 201302.

[41] Godehard Angloher et al. "Results from 730 kg days of the CRESST-II Dark Matter Search". In: *The European Physical Journal C* 72.4 (2012), p. 1971.

[42] K Abe et al. "XMASS detector". In: *Nuclear Instruments and Methods in Physics Research Section A: Accelerators, Spectrometers, Detectors and Associated Equipment* 716 (2013), pp. 78–85.

[43] Mark Guy Boulay, Deap Collaboration, et al. "DEAP-3600 dark matter search at SNOLAB". In: *Journal of Physics: Conference Series*. Vol. 375. 1. IOP Publishing. 2012, p. 012027.

[44] Elena Aprile et al. "The XENON dark matter search experiment". In: *New Astronomy Reviews* 49.2-6 (2005), pp. 289–295.

[45] DS Akerib et al. "The large underground xenon (LUX) experiment". In: *Nuclear Instruments and Methods in Physics Research Section A: Accelerators, Spectrometers, Detectors and Associated Equipment* 704 (2013), pp. 111–126.

[46] Andi Tan et al. "Dark matter results from first 98.7 days of data from the PandaX-II experiment". In: *Physical review letters* 117.12 (2016), p. 121303.

[47] P Agnes et al. "Low-mass dark matter search with the DarkSide-50 experiment". In: *Physical review letters* 121.8 (2018), p. 081307.

[48] André Rubbia. "ArDM: a ton-scale liquid Argon experiment for direct detection of Dark Matter in the Universe". In: *Journal of Physics: Conference Series*. Vol. 39. 1. IOP Publishing. 2006, p. 129.

[49] E. Aprile et al. "Dark Matter Search Results from a One Ton-Year Exposure of XENON1T". In: *Phys. Rev. Lett.* 121 (11 2018), p. 111302. DOI: 10.1103/PhysRevLett.121.111302. URL: https://link.aps.org/doi/10.1103/PhysRevLett.121.111302.

[50] Elena Aprile, Xenon Collaboration, et al. "The XENONnT dark matter experiment". In: *APS April Meeting Abstracts*. 2017.

[51] DN McKinsey, LZ Collaboration, et al. "The LZ dark matter experiment". In: *Journal of Physics: Conference Series*. Vol. 718. 4. IOP Publishing. 2016, p. 042039.

[52] CE Aalseth et al. "DarkSide-20k: A 20 tonne two-phase LAr TPC for direct dark matter detection at LNGS". In: *The European Physical Journal Plus* 133.3 (2018), p. 131.

[53] Laura Baudis et al. "A dual-phase xenon TPC for scintillation and ionisation yield measurements in liquid xenon". In: *The European Physical Journal C* 78.5 (2018), p. 351. ISSN: 1434-6052. DOI: 10.1140/epjc/s10052-018-5801-5. URL: https://doi.org/10.1140/epjc/s10052-018-5801-5.

[54] Hamamatsu Photonics K.K. *Photomultiplier Tubes - Basics and Applications*. 2017.

[55] Slawomir S. Piatek. *What is an SiPM and how does it work?* 2016. URL: https://hub.hamamatsu.com/jp/en/technical-note/how-sipm-works/index.html.

[56] M. Wang et al. "The AME2012 atomic mass evaluation (II). Tables, graphs and references". In: *Chin.Phys.C* 36 (2012), p. 1603.

[57] A Manalaysay et al. "Spatially uniform calibration of a liquid xenon detector at low energies using K 83 mr". In: *Review of Scientific Instruments* 81.7 (2010), p. 073303.

[58] Francesco Piastra. "Materials Radioassay for the XENON1T Dark Matter Experiment, and Development of a Time Projection Chamber for the Study of Low-energy Nuclear Recoils in Liquid Xenon". PhD thesis. Universität Zürich, 2017.

[59] Chamberlain Fong. "Analytical methods for squaring the disc". In: *arXiv preprint arXiv:1509.06344* (2015).

[60] Peter Sorensen. "Anisotropic diffusion of electrons in liquid xenon with application to improving the sensitivity of direct dark matter searches". In: *Nuclear Instruments and Methods in Physics Research Section A: Accelerators, Spectrometers, Detectors and Associated Equipment* 635.1 (2011), pp. 41–43.